Journal of Hazardous Materials 283 (2015) 787–805

Contents lists available at ScienceDirect

Journal of Hazardous Materials

journal homepage: www.elsevier.com/locate/jhazmat

Controlled hydrothermal synthesis of BiO_xCl_y/BiO_mI_n composites exhibiting visible-light photocatalytic degradation of crystal violet

Yu-Rou Jiang [a], Ho-Pan Lin [a], Wen-Hsin Chung [b], Yong-Ming Dai [a], Wan-Yu Lin [b], Chiing-Chang Chen [a,*]

[a] Department of Science Application and Dissemination, National Taichung University of Education, Taichung 403, Taiwan, ROC
[b] Department of Plant Pathology, National Chung Hsing University, Taichung 402, Taiwan, ROC

HIGHLIGHTS

- This is the first report on a series of BiO_xCl_y/BiO_mI_n heterojunctions.
- The BiO_xCl_y/BiO_mI_n composition was controlled by adjusting the growth parameters.
- The BiO_xCl_y/BiO_mI_n were indirect semiconductors with a 1.78–2.95-eV bandgap.
- The new photocatalysts removed CV at a much faster rate than TiO_2.
- Mechanisms were determined by separating the intermediates using HPLC-MS.

ARTICLE INFO

Article history:
Received 8 March 2014
Received in revised form 10 October 2014
Accepted 13 October 2014
Available online 29 October 2014

Keywords:
Photocatalysis
BiO_xCl_y/BiO_mI_n
Composites
Crystal violet
Hydrothermal synthesis

ABSTRACT

A series of BiO_xCl_y/BiO_mI_n composites were prepared using autoclave hydrothermal methods. The composition and morphologies of the BiO_xCl_y/BiO_mI_n composites were controlled by adjusting the experimental conditions: the reaction pH value, temperature, and KCl/KI molar ratio. The products were characterized using X-ray diffraction, scanning electron microscopy-electron dispersive X-ray spectroscopy, UV–vis diffuse reflectance spectroscopy, Brunauer–Emmett–Teller specific surface areas, cathodoluminescence, high-resolution transmission electron microscopy, and high-resolution X-ray photoelectron spectroscopy. The photocatalytic efficiencies of composite powder suspensions were evaluated by monitoring the crystal violet (CV) concentrations. In addition, the quenching effects of various scavengers indicated that the reactive $O_2^{\bullet -}$ played a major role, and $OH^{\bullet}$ or h^+ played a minor role in CV degradation. The intermediates formed during the decomposition process were isolated, identified, and characterized using high performance liquid chromatography-photodiode array-electrospray ionization-mass spectrometry to elucidate the CV decomposition mechanism.

1. Introduction

The elimination of toxic chemicals from wastewater has become one of the most crucial aspects of contemporary pollution-control methods because of the hazardous effects of these chemicals on living beings and the environment. In particular, triphenylmethane (TPM) dyes are extensively used in the leather, cosmetic, paper, and food industries as coloring agents for plastics, oils, fats, waxes, and varnishes [1]. The photocytotoxicity of TPM dyes, which is caused by the production of reactive oxygen species, has been intensively studied because of the potential applications of these dyes in photodynamic treatments [2]. However, the thyroid peroxidase-catalyzed oxidation of TPM dyes in living organisms is of great concern because the oxidation reactions can produce various *N*-dealkylated aromatic amines with structures similar to those of carcinogenic aromatic amines [3]. Recent reports have indicated that TPM dyes can serve as targetable sensitizers in the photodecomposition of specific cells or cellular components [2,3].

In recent years, photocatalytic processes have been successfully used to degrade TPM dye pollutants [4]. Crystal violet (CV) decomposition has been studied using several systems that generate active species, including $Bi_xAg_yO_z$ [5], Bi_2WO_6 [6], TiO_2 [7], ZnO [8], and $BaTiO_3$ [9]. In most cases, the reaction mechanisms, kinetics, and efficiency have been well documented.

* Corresponding author. Tel.: +886 4 2218 3406; fax: +886 4 2218 3560.
E-mail addresses: ccchen@ms3.ntcu.edu.tw, ccchen@mail.ntcu.edu.tw (C.-C. Chen).

http://dx.doi.org/10.1016/j.jhazmat.2014.10.025
0304-3894/

Recently, the development of visible-light-sensitive photocatalysts has received considerable attention as an alternative for wastewater treatment. A new class of promising photocatalysts, bismuth oxyhalides [10,11], has recently been demonstrated to possess remarkable photocatalytic activity; bismuth oxyhalides belong to the group V-VI-VII family of multicomponent metal oxyhalides. Their photocatalytic activity results from their unique layered structure, which has an internal static electric field perpendicular to each layer. The electric field can effectively separate photogenerated electron–hole pairs.

A simple and effective strategy to improve the photocatalytic activity of a photocatalyst is to incorporate a heterostructure (or composites), because heterojunctions (or composites) have high potential for favorably modifying the electronic properties of composite photocatalysts and efficiently separating photogenerated electron–hole pairs [12]. Following the report of Keller and Kramer [13], who first studied the practically unlimited solubility of the BiOX/BiOY (X, Y = Cl, Br, I) system, several articles have reported the successful synthesis of similar oxyhalide materials with unique photocatalytic properties. Xiao et al. [14] reported the synthesis of BiOI/BiOCl phases exhibiting high photocatalytic activities under visible light irradiation for the degradation of bisphenol A and methyl orange. Dong et al. [15] prepared BiOCl/BiOI photocatalysts through a coprecipitation method and observed that, under visible light irradiation, a new photoactive material with $x = 0.25$ removed NO four times faster than P25-TiO_2 did. Diffuse reflectance spectra analysis results and observations of large generated photocurrents have recently suggested that BiOCl/BiOI absorbs visible light, which enhances the generation and separation of electron–hole pairs [15].

This paper details the preparation and characterization of a series of BiO_xCl_y/BiO_mI_n photocatalysts, and it is the first paper to present a systematic synthetic study of BiO_xCl_y/BiO_mI_n based on autoclave hydrothermal methods. The photocatalytic activities of BiO_xCl_y/BiO_mI_n, which exhibit excellent photocatalytic activity under visible light irradiation, were evaluated by measuring the degradation rate of CV and phenol. A new photoactive material removes aqueous CV under visible light irradiation at a much faster rate than P25-TiO_2 does. The intermediates in the process were isolated, identified, and characterized using high performance liquid chromatography-photodiode array-electrospray ionization-mass spectrometry (HPLC-PDA-ESI-MS) to elucidate the CV decomposition mechanism.

2. Experimental details

2.1. Materials

$Bi(NO_3)_3{\cdot}5H_2O$, KI (Katayama), KCl (Shimakyu), CV dye (TCI), *p*-benzoquinone (Alfa Aesar), sodium azide (Sigma), ammonium oxalate (Osaka), and isopropanol (Merck) were purchased and used without further purification. Reagent-grade sodium hydroxide, nitric acid, ammonium acetate, and HPLC-grade methanol were obtained from Merck. Deionized water was purified using a Milli-Q water ion-exchange system (Millipore Co.) to attain a resistivity of $1.8 \times 10^7\ \Omega$ cm.

2.2. Instruments and analytical methods

X-ray diffraction (XRD) patterns were recorded on an MAC Science MXP18 diffractometer system with Cu Kα radiation, operating at 40 kV and 80 mA. Field emission-scanning electron microscopy-electron dispersive X-ray spectroscopy (FE-SEM-EDS) measurements were obtained using a JEOL JSM-7401F microscope at an acceleration voltage of 15 kV. High-resolution X-ray photoelectron spectroscopy measurements were obtained using an ULVAC-PHI spectrometer. Field-emission transmission electron microscopy (FE-TEM) images, selected area electron diffraction patterns, high-resolution transmission electron microscopy (HRTEM) images, and energy-dispersive X-ray spectroscopy (EDS) spectra were obtained using a JEOL-2010 microscope at an acceleration voltage of 200 kV. The Al Kα radiation was produced at 15 kV. Cryogenic cathodoluminescence (CL) measurements were obtained using a JEOL JSM7001F microscope. The Brunauer–Emmett–Teller (BET) specific surface areas of the samples (S_{BET}) were measured using an automated system (Micromeritics Gemini, 237 °C); nitrogen gas was used as the adsorbate at liquid-nitrogen temperature. The HPLC-PDA-ESI-MS system consisted of a Waters 1525 binary pump, Waters 2998 photodiode array detector, and Waters 717 plus autosampler; a ZQ2000 micromass detector. The concentration of Cl^- and I^- ions in solution was determined through ion chromatography on a model 883 Basic IC plus ion chromatograph (Metrohm) by using a Metrosep A Supp 5–150 column and carbonate was used as the standard eluent.

2.3. Synthesis of BiO_xCl_y/BiO_mI_n

A 50-mL flask was charged with $Bi(NO_3)_3{\cdot}5H_2O$ (5 mmol), followed by the addition of 4 M HNO_3 (5 mL). Under continuous stirring, 2 M NaOH was added dropwise to adjust the pH value; when a precipitate was formed, 3 M KCl (2 mL) and KI (2 mL) were also added dropwise. The solution was vigorously stirred for 30 min and transferred to a 30-mL Teflon-lined autoclave, which was heated to 110–260 °C for 12 h and then allowed to cool to room temperature. The resulting solid was collected through filtration, washed with deionized water and methanol to remove any ionic species, and then dried at 60 °C overnight. Depending on the KCl/KI molar ratio (2:1, 1:2), pH value, temperature, and reaction times, the BiO_xCl_y/BiO_mI_n composites were synthesized and labeled as shown in Table 1; the as-prepared samples were labeled from BC1I2-1-110-12 to BC2I1-260-12.

2.4. Photocatalytic experiments

CV irradiation experiments were conducted on stirred aqueous solutions contained in a 100-mL flask; an aqueous suspension of CV (100 mL, 10 ppm) and the catalyst powder were placed in a Pyrex flask. The pH value of the suspension was adjusted by adding either NaOH or HNO_3 solution. Dark (sorption) experiments were performed to examine the adsorption–desorption equilibrium. Ten milligrams of the photocatalyst was mixed with 100 mL of aqueous CV solution with a known initial concentration, in a 100 mL flask and the mixture was shaken in an orbital shaker (100 rpm) at a constant temperature. After batch sorption experiments were conducted, the mixture was centrifuged at 3000 rpm in a centrifugation machine for determining the absorbance of CV at 588.3 nm through HPLC-PDA-ESI-MS. The concentrations of the solutions were determined using a linear regression equation. Before irradiation, the suspension was magnetically stirred in the dark for approximately 30 min to establish the adsorption–desorption equilibrium between the dye and the catalyst surface. Irradiation conducted using 150-W Xe arc lamps; the light intensity was fixed at 32.1 W/m^2, and the reaction vessel was placed 30 cm from the light source. At given irradiation time intervals, a 5-mL aliquot was collected and centrifuged to remove the catalyst. The supernatant was analyzed through HPLC-PDA-ESI-MS.

Table 1
Codes of BiO_xCl_y/BiO_mI_n prepared under different KCl/KI molar ratio, pH values, and reaction temperatures at 12 h.

pH	T (°C)			
	110	160	210	260
BC1I2				
1	BC1I2-1-110-12	BC1I2-1-160-12	BC1I2-1-210-12	BC1I2-1-260-12
4	BC1I2-4-110-12	BC1I2-4-160-12	BC1I2-4-210-12	BC1I2-4-260-12
7	BC1I2-7-110-12	BC1I2-7-160-12	BC1I2-7-210-12	BC1I2-7-260-12
10	BC1I2-10-110-12	BC1I2-10-160-12	BC1I2-10-210-12	BC1I2-10-260-12
13	BC1I2-13-110-12	BC1I2-13-160-12	BC1I2-13-210-12	BC1I2-13-260-12
BC2I1				
1	BC2I1-1-110-12	BC2I1-1-160-12	BC2I1-1-210-12	BC2I1-1-260-12
4	BC2I1-4-110-12	BC2I1-4-160-12	BC2I1-4-210-12	BC2I1-4-260-12
7	BC2I1-7-110-12	BC2I1-7-160-12	BC2I1-7-210-12	BC2I1-7-260-12
10	BC2I1-10-110-12	BC2I1-10-160-12	BC2I1-10-210-12	BC2I1-10-260-12
13	BC2I1-13-110-12	BC2I1-13-160-12	BC2I1-13-210-12	BC2I1-13-260-12

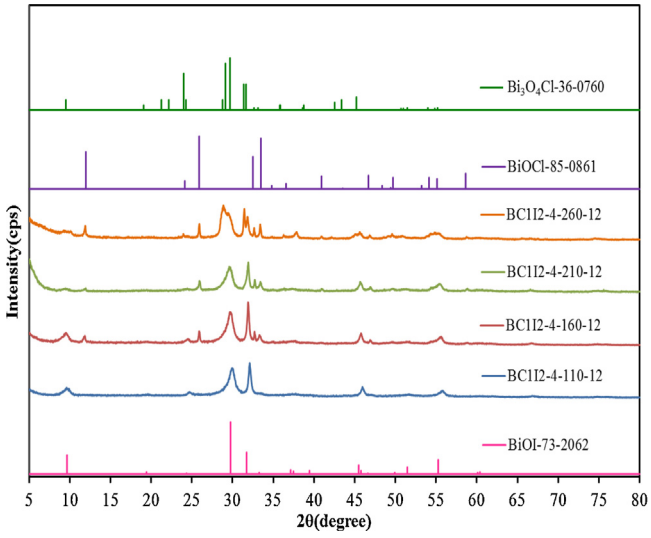

Fig. 1. XRD patterns of as-prepared BiO_xCl_y/BiO_mI_n samples at various temperatures (KCl/KI molar ratio = 1/2; hydrothermal conditions: temp = 110–260 °C, pH = 4, time = 12 h).

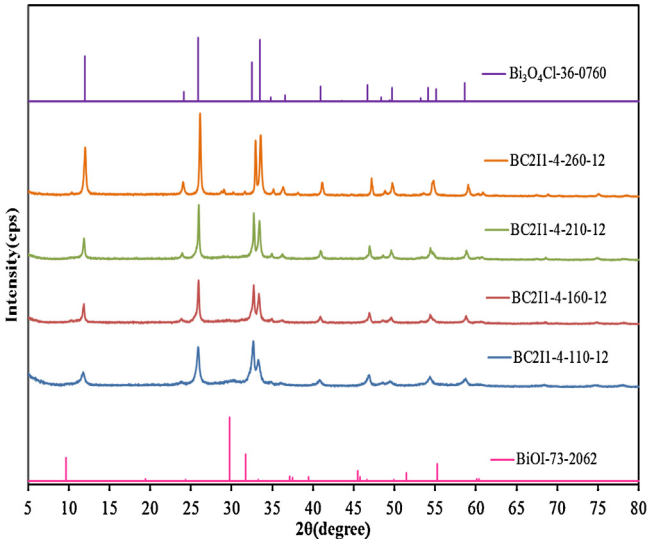

Fig. 2. XRD patterns of as-prepared BiO_xCl_y/BiO_mI_n samples at various temperatures (KCl/KI molar ratio = 2/1; hydrothermal conditions: temp = 110–260 °C, pH = 4, time = 12 h).

3. Results and discussion

3.1. Characterization of BiO_xCl_y/BiO_mI_n composites

3.1.1. Phase structure

Figs. 1 and 2 and Figs. S1–S8 (Supplementary Materials) show XRD patterns of the as-prepared samples; the patterns clearly reveal the coexistence of distinct phases. All the as-prepared samples contained the BiOCl phase (JCPDS 85-0861) in addition to the Bi_3O_4Cl (JCPDS 36-0760), $Bi_{12}O_{17}Cl_2$ (JCPDS 37-0702), BiOI (JCPDS 73-2062), $Bi_7O_9I_3$ [16], and Bi_5O_7I (JCPDS 40-0548) phases. XRD patterns for pH values of 1, 4, 7, 10, and 13 were identical to those reported for the BiOCl/BiOI, $Bi_3O_4Cl/Bi_7O_9I_3$, and $Bi_{12}O_{17}Cl_2/Bi_5O_7I$ binary phases and $BiOCl/Bi_3O_4Cl/BiOI$ and $BiOCl/Bi_{12}O_{17}Cl_2/Bi_7O_9I_3$ ternary phases. Table 2 summarizes the results of the XRD measurements.

Figs. 3–6 show that BC1I2-4-160-12, BC1I2-7-160-12, BC1I2-10-160-12, and BC2I1-7-160-12 were composed of sheets or plates of various sizes, consistent with TEM observations. In addition, the EDS spectrum shows that the sample contained elemental Bi, O, Cl, and I. The Cl (or I) atomic ratio of the samples was within the range of 2.49% to 7.95% (or 15.05–8.56%), corresponding to various heterojunctions. The HRTEM image reveals that two sets of lattice images were obtained with d-spacings of 0.275, 0.309, and 0.241 nm, corresponding to the (1 1 0) plane of BiOCl, (6 0 0) plane of Bi_3O_4Cl, and (0 1 3) plane of BiOI (Fig. 3), respectively.

Table 2
Crystalline phase changes of BiO_xCl_y/BiO_mI_n nanosheets prepared under different reaction conditions.

(○BiOI; □$Bi_7O_9I_3$; ▽Bi_5O_7I; ●BiOCl; ◆Bi_3O_4Cl; ●$Bi_{12}O_{17}Cl_2$)

BC1I2				
T(°C) / pH	110	160	210	260
1	○●	○●	○●	○●
4	○●	○●◆	○●◆	○●◆
7	□◆	□◆	□◆	□◆
10	▽●	▽●	▽●	▽●
13	▽●	▽●	▽●	▽●
BC2I1				
T(°C) / pH	110	160	210	260
1	○●	○●	○●	○●
4	○◆	○◆	○◆	○◆
7	□●●	□●●	□●●	□●●
10	▽●	▽●	▽●	▽●
13	▽●	▽●	▽●	▽●

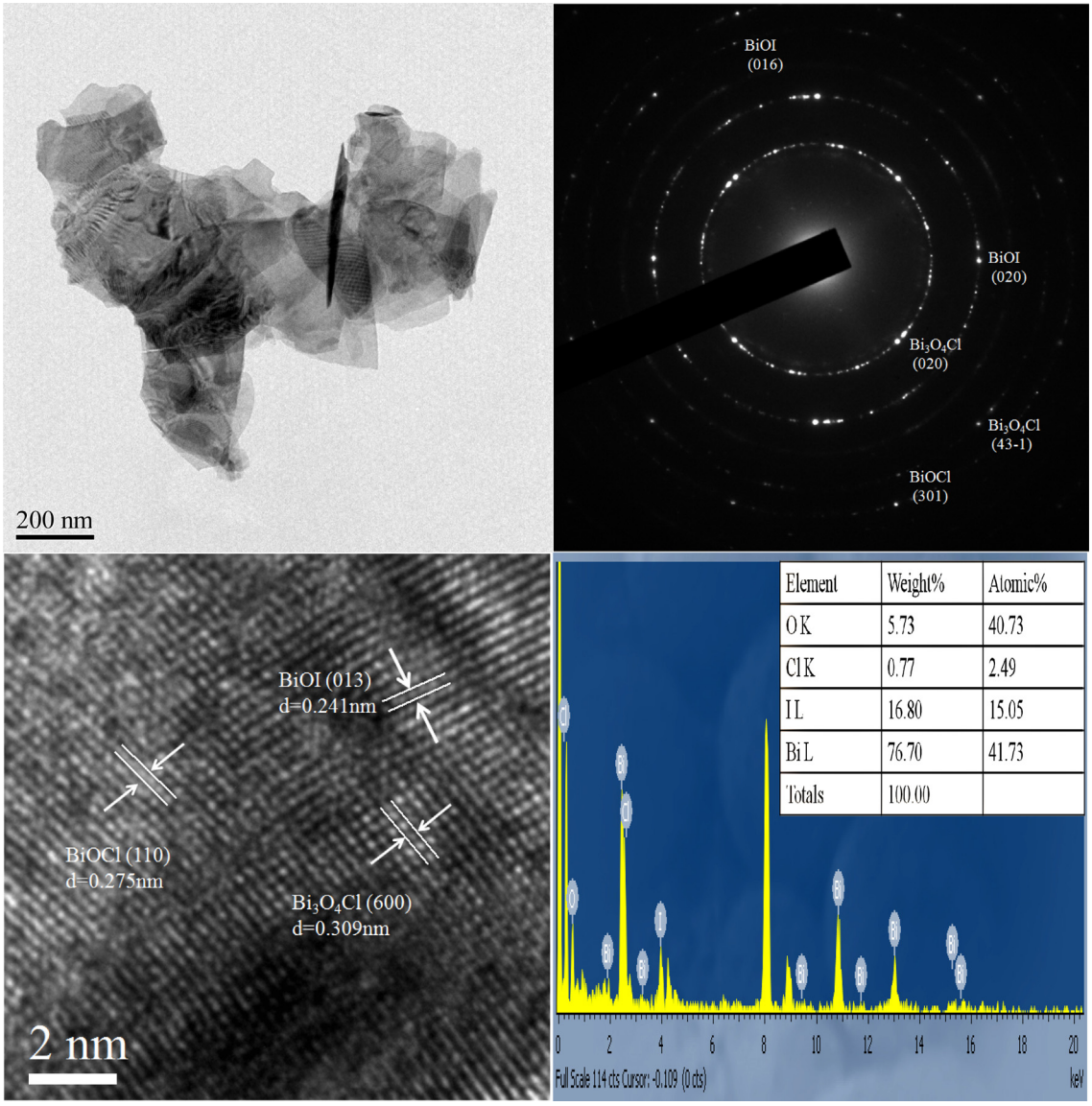

Fig. 3. FE-TEM images and EDS of the BC1I2-4-160-12 sample prepared using the autoclave hydrothermal method.

The d-spacings of 0.365 and 0.281 nm corresponded to the (2 1 1) plane of Bi_3O_4Cl and (1 1 0) plane of $Bi_7O_9I_3$, respectively (Fig. 4). The d-spacings of 0.305 and 0.317 nm corresponded to the (1 1 7) plane of $Bi_{12}O_{17}Cl_2$ and (3 1 2) plane of Bi_5O_7I (Fig. 5), respectively. The d-spacings of 0.166, 0.192, and 0.206 nm corresponded to the (1 0 4) plane of BiOCl, (2 2 0) plane of $Bi_{12}O_{17}Cl_2$, and (1 1 3) plane of $Bi_7O_9I_3$ (Fig. 6), respectively, which is in strong agreement with the XRD results. The results suggest that the BiOCl/Bi_3O_4Cl/BiOI, Bi_3O_4Cl/$Bi_7O_9I_3$, $Bi_{12}O_{17}Cl_2$/Bi_5O_7I, and BiOCl/$Bi_{12}O_{17}Cl_2$/$Bi_7O_9I_3$ phases were formed in the composites; the formation of these phases was favorable for the separation of photoinduced carriers, which resulted in high photocatalytic activities.

The results showed that at various pH values in hydrothermal reactions, a series of changes occurred in the compounds; the changes can be described as BiOCl → $Bi_4O_5Cl_2$ → $Bi_{24}O_{31}Cl_{10}$ → Bi_3O_4Cl → $Bi_{12}O_{17}Cl_2$ → α-Bi_2O_3 and BiOI → $Bi_4O_5I_2$ → $Bi_7O_9I_3$ → Bi_3O_4I → Bi_5O_7I → α-Bi_2O_3. Possible processes for the formation of BiO_xCl_y/BiO_mI_n samples are presented in Eqs. (1)–(17).

$$Bi^{3+} + 3OH^- \rightarrow Bi(OH)_3(s) \quad (1)$$

$$Bi(OH)_3(s) + 3Cl^- \rightarrow BiCl_3(s) + 3OH^- \quad (2)$$

$$BiCl_3(s) + 2OH^- \rightarrow BiOCl(s) + 2Cl^- + H_2O \quad (3)$$

$$4BiOCl(s) + 2OH^- \rightarrow Bi_4O_5Cl_2(s) + 2Cl^- + H_2O \quad (4)$$

$$6Bi_4O_5Cl_2(s) + 2OH^- \rightarrow Bi_{24}O_{31}Cl_{10}(s) + 2Cl^- + H_2O \quad (5)$$

$$Bi_{24}O_{31}Cl_{10}(s) + 2OH^- \rightarrow 8Bi_3O_4Cl(s) + 2Cl^- + H_2O \quad (6)$$

$$5Bi_3O_4Cl(s) + 2OH^- \rightarrow 3Bi_5O_7Cl(s) + 2Cl^- + H_2O \quad (7)$$

$$12Bi_5O_7Cl(s) + 2OH^- \rightarrow 5Bi_{12}O_{17}Cl_2(s) + 2Cl^- + H_2O \quad (8)$$

$$Bi_{12}O_{17}Cl_2(s) + 2OH^- \rightarrow 6Bi_2O_3(s) + 2Cl^- + H_2O \quad (9)$$

$$Bi(OH)_3(s) + I^- \rightarrow BiOI(s) + H_2O + OH^- \quad (10)$$

$$Bi^{3+} + 3I^- \rightarrow BiI_3(s) \quad (11)$$

$$BiI_3(s) + 2OH^- \rightarrow BiOI(s) + 2I^- + H_2O \quad (12)$$

$$4BiOI(s) + 2OH^- \rightarrow Bi_4O_5I_2(s) + 2I^- + H_2O \quad (13)$$

$$7Bi_4O_5I_2(s) + 2OH^- \rightarrow 4Bi_7O_9I_3(s) + 2I^- + H_2O \quad (14)$$

$$3Bi_7O_9I_3(s) + 2OH^- \rightarrow 7Bi_3O_4I(s) + 2I^- + H_2O \quad (15)$$

$$5Bi_3O_4I(s) + 2OH^- \rightarrow 3Bi_5O_7I(s) + 2I^- + H_2O \quad (16)$$

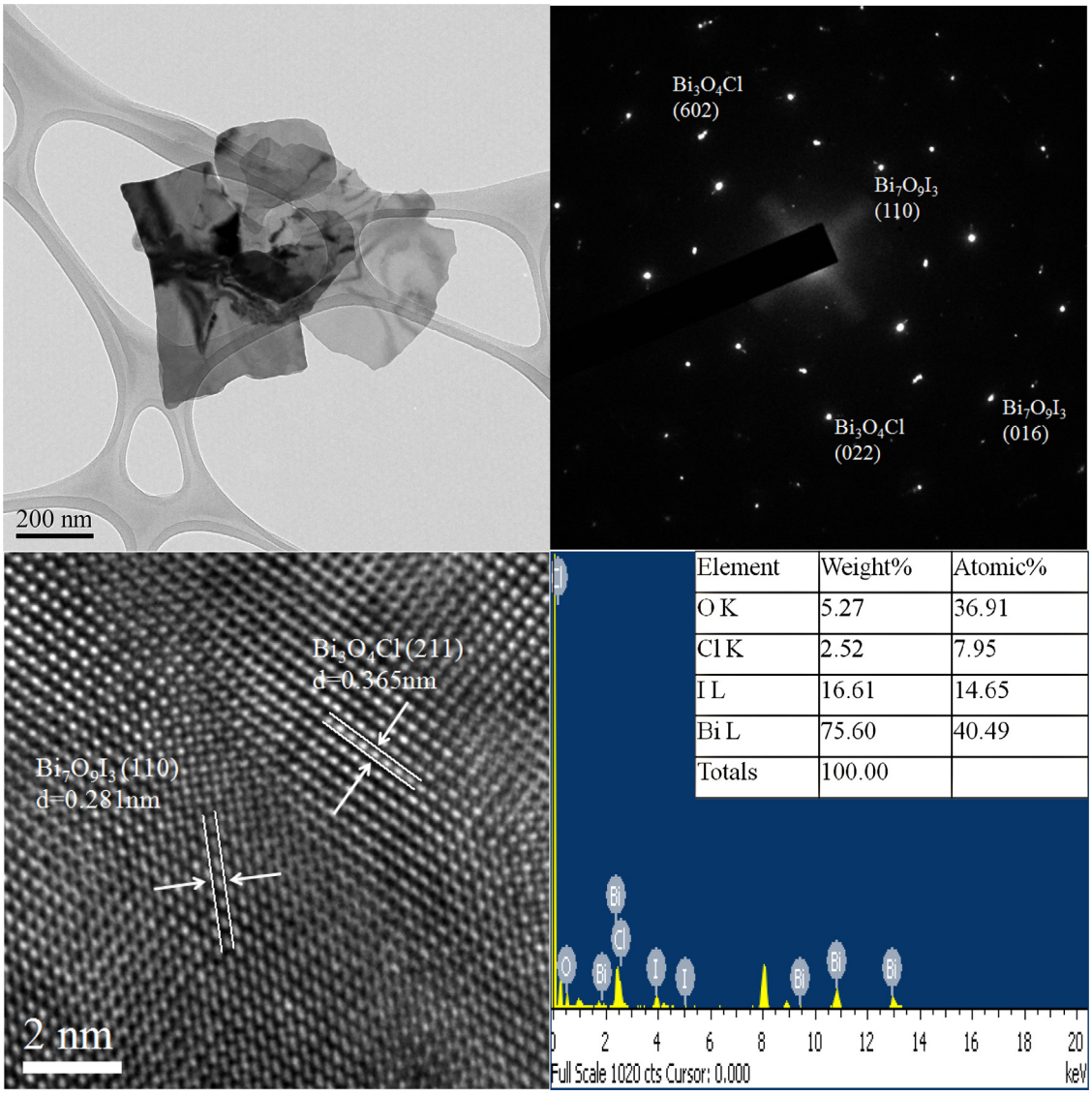

Fig. 4. FE-TEM images and EDS of the BC1I2-7-160-12 sample prepared using the autoclave hydrothermal method.

$$2Bi_5O_7I(s) + 2OH^- \rightarrow 5Bi_2O_3(s) + 2I^- + H_2O \quad (17)$$

These equations show that BiOCl (or BiOI) was formed at the beginning of the reaction and then OH^- gradually substituted Cl^- (or I^-) under the basic conditions, which resulted in the reduced amount of Cl^- (or I^-) in the products. The concentrations of Cl^- and I^- were confirmed using ion chromatography (IC), based on their retention times [17,18]. An alternative approach for tracking the progress of the hydrothermal synthesis of BiO_xCl_y/BiO_mI_n, which is a halo-semiconductor, is to monitor the chloride and iodide ions formed in the solution. The concentrations of Cl^- and I^- ions as a function of the reaction at various pH values are shown in Fig. S9. IC analysis showed an increase in the Cl^- and I^- concentrations at various pH values as the hydrothermal method progressed. These results indicated that Cl^- and I^- were gradually displaced by OH^- as the pH value gradually increased. The pH value was gradually increased to obtain $Bi_4O_5Cl_2$, $Bi_{24}O_{31}Cl_{10}$, Bi_3O_4Cl, Bi_5O_7Cl, $Bi_{12}O_{17}Cl_2$ (or $Bi_4O_5I_2$, $Bi_7O_9I_3$, Bi_3O_4I, and Bi_5O_7I), and α-Bi_2O_3. The higher the pH value was, the lower the Cl^- (or I^-) content of the products was. Finally, the Cl^- (or I^-) ions in the products were fully replaced by OH^- ions, resulting in the formation of α-Bi_2O_3 under strong basic conditions. A competitive relationship typically existed between OH^-, Cl^-, and I^- ions in the aqueous solution. Thus, the selective preparation of BiO_xCl_y/BiO_mI_n through the adjustment of the pH value in the hydrothermal method was demonstrated.

3.1.2. Morphological structure and composition

BiO_xCl_y/BiO_mI_n was prepared from $Bi(NO_3)_3{\cdot}5H_2O$ and a mixture of KCl and KI by using hydrothermal methods at 110 °C and at pH 4, 7, 9, and 13. The surface morphologies of the photocatalysts were examined using FE-SEM-EDS (Figs. 7 and 8). Table 2 shows that as the pH value increased from 1 to 13, a gradual change occurred in the crystal phases of the reflection peaks, indicating the formation of a variety of compounds in the crystalline phase. These compounds included BiOCl/BiOI, BiOCl/Bi_3O_4Cl/BiOI, $Bi_3O_4Cl/Bi_7O_9I_3$, $Bi_{12}O_{17}Cl_2/Bi_5O_7I$, and BiOCl/$Bi_{12}O_{17}Cl_2/Bi_7O_9I_3$ composites and α-Bi_2O_3. In Figs. 7 and 8, the FE-SEM-EDS image shows that the morphology of the samples obtained at a KCl/KI molar ratio of 1:2 and 2:1, respectively at various pH values changed from irregular sheets to irregular multisheets, before changing to microrectangular/pillar crystals (or flower-like crystals to thin sheets, irregular multisheets, and finally to microrectangular/pillar crystals). These samples displayed irregular nanosheet structures with widths of up to 70 μm and thicknesses in the range of 5–50 nm; the rectangular-pillar crystals showed similar

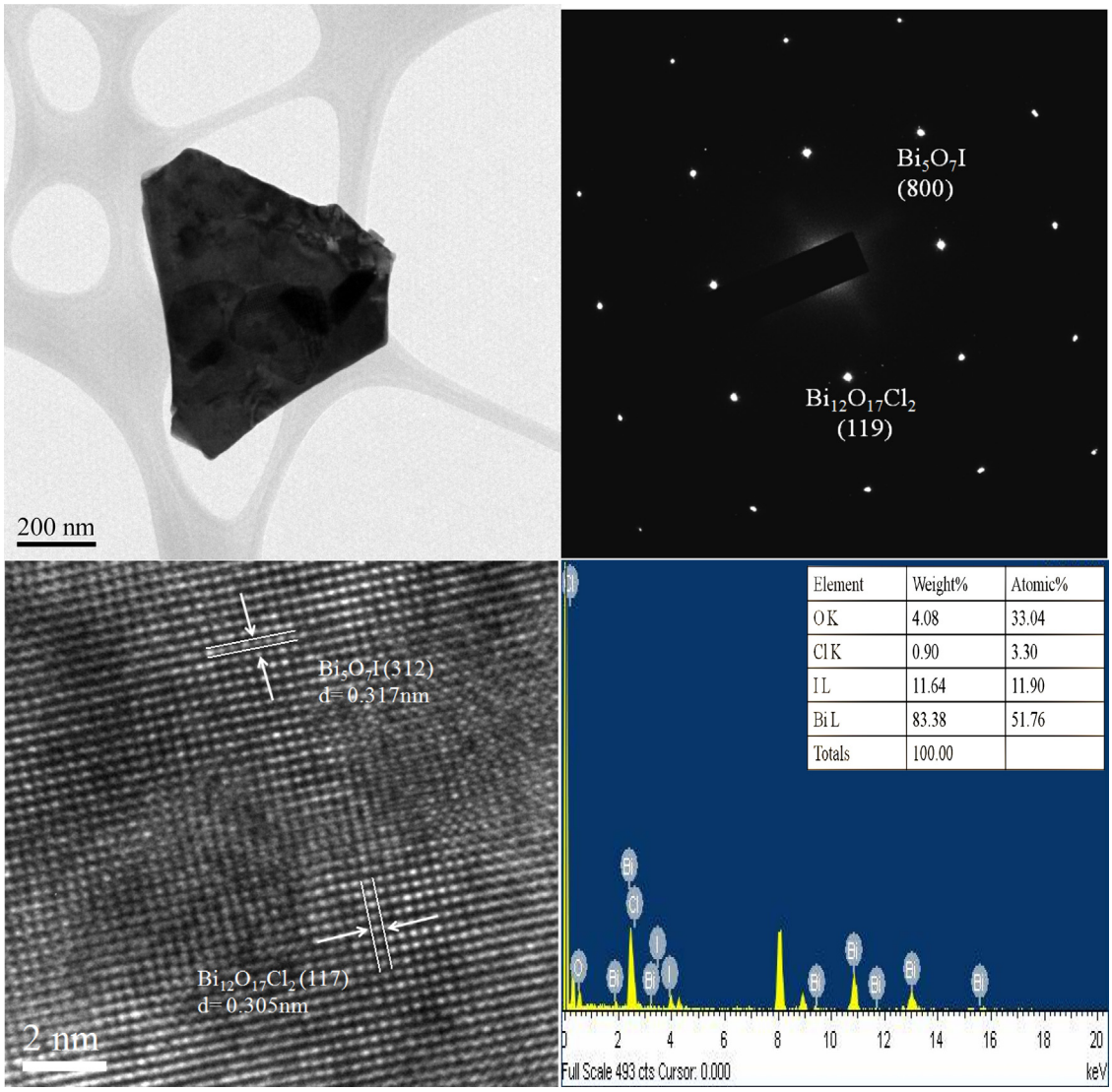

Fig. 5. FE-TEM images and EDS of the BC1I2-10-160-12 sample prepared using the autoclave hydrothermal method.

dimensions. BiOX (X = F, Cl, Br, I) is characterized by a layered structure in which halogen atoms are situated between $[Bi_2O_2]$ layers [19]. The internal electric fields between the $[Bi_2O_2]^{2+}$ positive layers and the negative halogen layers are believed to effectively separate photogenerated electron–hole pairs, thus enhancing the photocatalytic activity of the catalysts [20]. The SEM-EDS and TEM-EDS results showed that the main elements within these samples were bismuth, chlorine, iodine, and oxygen at various pH values (Table 3 and Figs. 3–6). In Table 3, the EDS results show that the main elements of these samples were bismuth, chlorine, iodine, and oxygen at various pH values. The Cl (or I) atomic ratios (%) of the samples were within the range 15.91–1.21 (or 18.40–5.95),

Table 3
Physical and chemical properties of BiO_xCl_y/BiO_mI_n.

Catalyst code	EDS of atomic ratio (%)				XPS of atomic ratio (%)				E_g (eV)
	Bi	O	Cl	I	Bi	O	Cl	I	
BC1I2-1-110-12	32.67	37.76	11.17	18.40	59.9	24.5	12.0	3.6	1.78
BC1I2-4-110-12	33.15	41.45	8.74	16.65	75.9	15.0	5.7	3.4	2.07
BC1I2-7-110-12	36.01	45.44	5.68	12.86	83.3	10.9	3.0	2.8	2.20
BC1I2-10-110-12	31.13	47.65	3.40	7.82	76.8	18.2	1.1	2.1	2.37
BC1I2-13-110-12	29.12	63.71	1.21	5.95	62.8	31.5	0.1	1.5	2.91
BC2I1-1-110-12	26.26	45.74	15.91	11.99	63.0	19.0	10.2	8.99	2.08
BC2I1-4-110-12	32.49	49.60	8.98	8.93	62.6	22.5	9.3	8.93	2.13
BC2I1-7-110-12	28.63	57.81	6.33	7.22	70.5	22.5	3.6	7.22	2.16
BC2I1-10-110-12	36.19	54.67	2.76	6.38	68.6	27.2	1.3	6.38	2.45
BC2I1-13-110-12	29.34	60.74	3.94	5.98	52.2	42.8	0.3	5.98	2.95
BC3-1-110-12	30.67	41.80	27.53	N/A	38.3	32.3	29.5	N/A	3.10
BI3-1-110-12	24.47	50.22	N/A	25.31	80.3	11.9	N/A	7.8	1.57

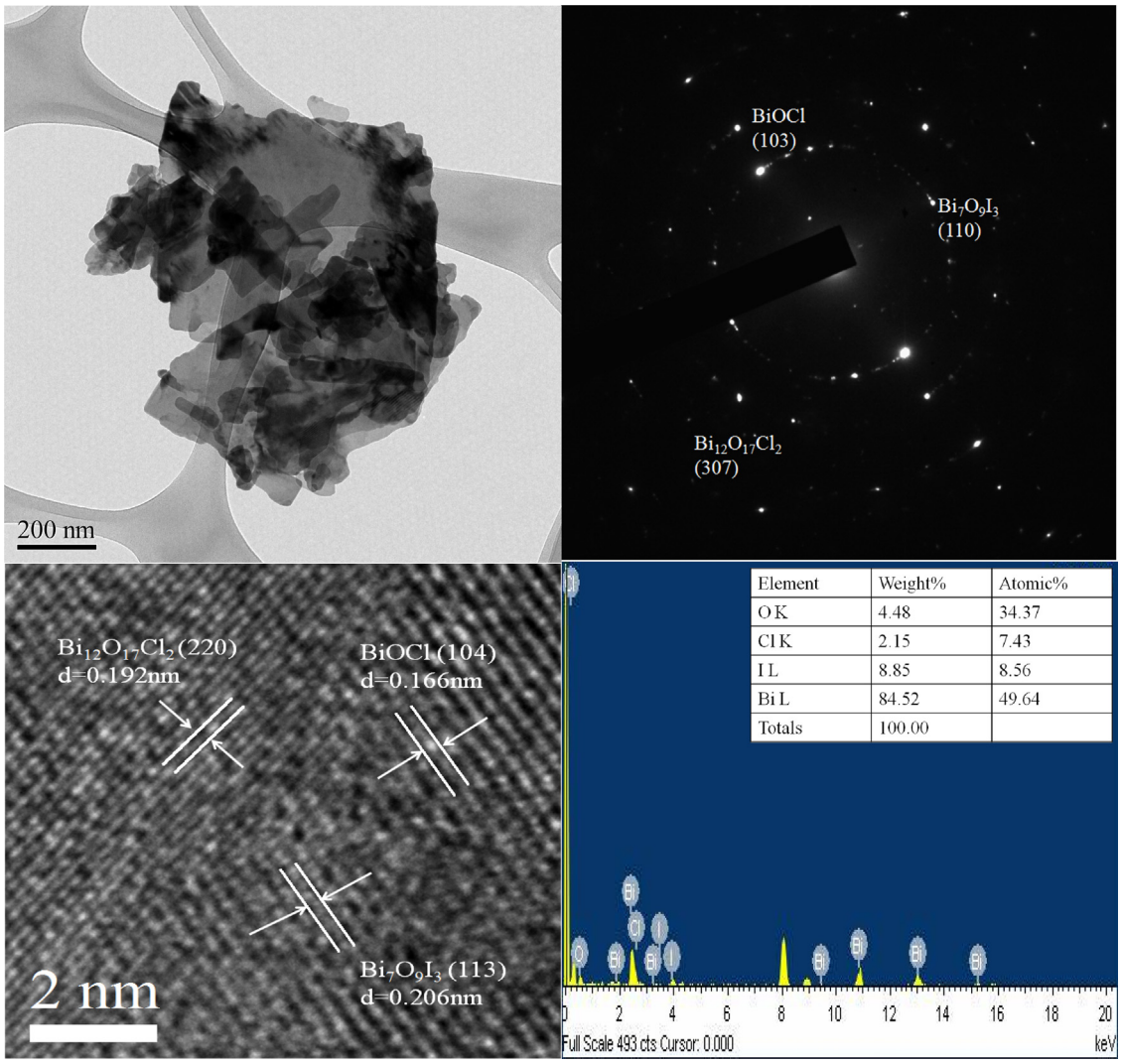

Fig. 6. FE-TEM images and EDS of the BC2I1-7-160-12 sample prepared using the autoclave hydrothermal method.

which corresponded to $Bi_4O_5Cl_2$, $Bi_{24}O_{31}Cl_{10}$, Bi_3O_4Cl, Bi_5O_7Cl, and $Bi_{12}O_{17}Cl_2$ (or $Bi_4O_5I_2$, $Bi_7O_9I_3$, Bi_3O_4I, and Bi_5O_7I) and Bi_2O_3 and their mixture phase, unlike the stoichiometric ratio (Bi:Cl = 1, 2, 2.4, 3, 5, and 6, respectively; Bi:I = 1, 2, 2.3, and 5, respectively), and could be selectively prepared using a facile solution-based hydrothermal method. The detailed morphological structure and composition are described in the supplementary materials.

3.1.3. X-ray photoelectron spectroscopy analysis

XPS was employed to examine the purity of the prepared samples; the spectra are presented in Figs. 9 and S10 and Table 3. Figs. 9 and S10 show the Bi 4f, Cl 2p, I 3d, and O 1s XPS spectra for the five BiO_xCl_y/BiO_mI_n samples. The transition peaks involving the Bi 4f, Cl 2p, I 3d, O 1s, and C 1s orbitals indicate that the catalysts were composed of Bi, O, Cl, I, and C (Figs. 9(a) and 10(a)). The detailed XPS data are described in Supplementary Materials. The XPS results revealed that the suggested processes for the formation of BiO_xCl_y/BiO_mI_n are consistent with previous results obtained through XRD and TEM analyses.

3.1.4. Optical absorption properties

DR-UV of the various catalysts is shown in Fig. 10(a). BiOCl absorbed only a small amount of visible light, whereas the absorption edge of BiOI extended across the entire visible light spectrum. Moreover, the absorption edges of BiO_xCl_y/BiO_mI_n showed the monotonic red-shift response of BiO_xCl_y. By using the absorption spectra of semiconductors, the E_g value of the semiconductors can be calculated from the expression $\alpha h\nu = A(h\nu - E_g)^{n/2}$. The values of n for BiOCl and BiOI are 4 and 4, respectively [21]. The E_g value of BiO_xCl_y/BiO_mI_n was determined from a plot of $(\alpha h\nu)^{1/2}$ versus energy ($h\nu$) (Fig. 10(b)), and it was determined to be in the range of 1.78–2.95 eV (Table 3). The steep shape and strong absorption in the visible region can be ascribed to the intrinsic bandgap transition between the valence band and the conduction band, rather than transitions from impurity levels [22].

3.1.5. Adsorption–desorption isotherm, pore structure, and specific surface areas

Fig. 11(a) shows the nitrogen adsorption–desorption isotherm curves of BiO_xCl_y/BiO_mI_n at various pH values. The isotherms of all the samples are close to Type IV, with a hysteresis loop at a high relative pressure between 0.6 and 1.0 [23]. The shape of the hysteresis loop is close to Type H3, suggesting the existence of slit-like pores generally formed by the aggregation of plate-like particles; this suggestion is consistent with the self-assembled nanoplate-like morphology of the samples (Fig. 11(b)) [23]. This result is consistent with the FE-SEM results, which showed that self-assembled nanosheets or nanoplates formed 3D hierarchical

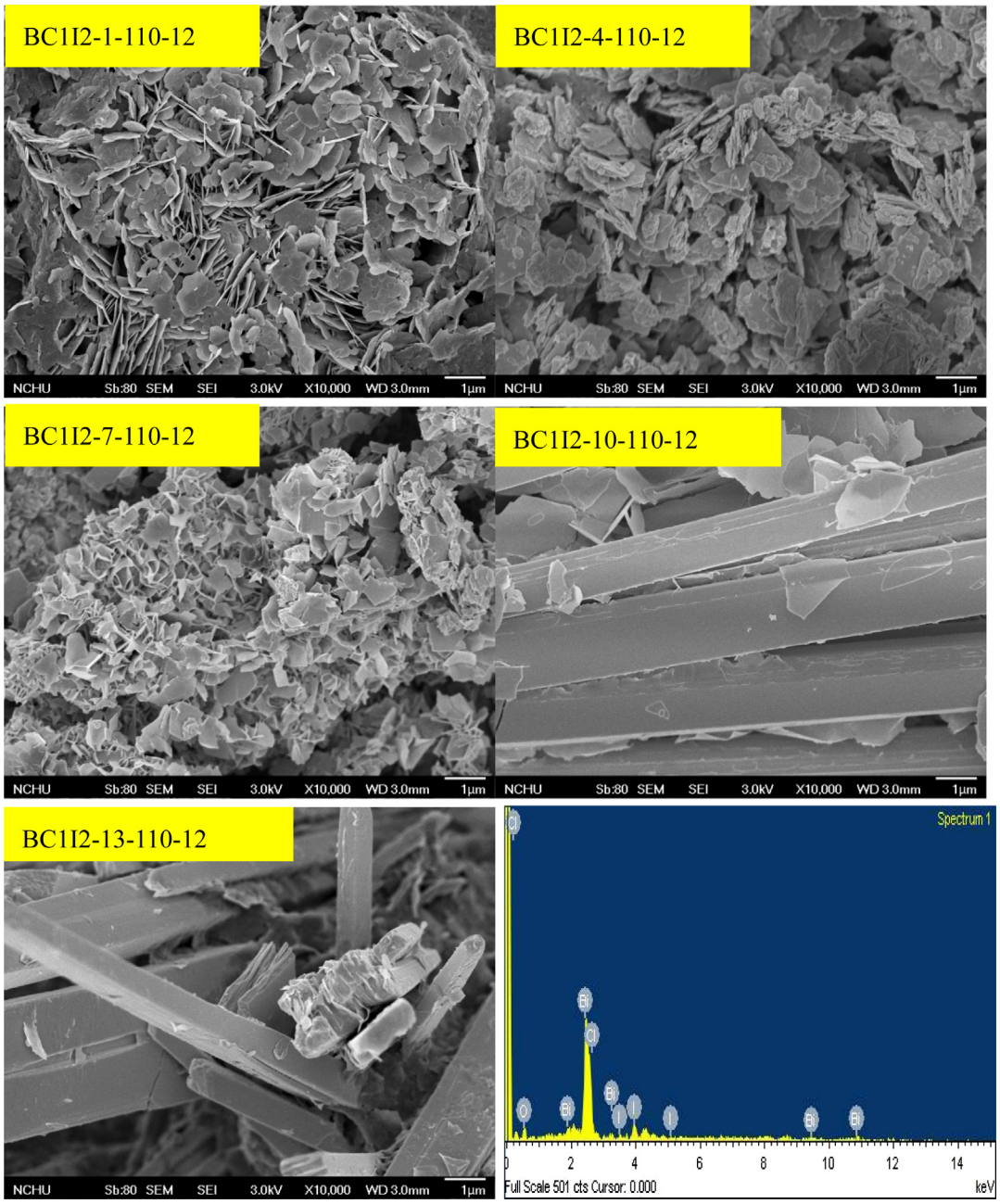

Fig. 7. SEM images of BiO_xCl_y/BiO_mI_n prepared using the autoclave hydrothermal method at various pH values (KCl/KI molar ratio = 1/2; hydrothermal conditions: temp = 110 °C, pH = 1–13, time = 12 h).

structures. Fig. S11 shows the corresponding pore-size distribution (PSD) of BiO_xCl_y/BiO_mI_n samples. The pore parameters of the BiO_xCl_y/BiO_mI_n samples are summarized in Table 4. The PSD of the samples has been described in the supplementary materials.

The S_{BET} value determined from BET isotherms of BiO_xCl_y/BiO_mI_n was approximately 0.54–16.68 m^2/g. This range is lower than that of P25-TiO_2 (35.4 m^2/g) because of the larger particle size (Table 4). A larger S_{BET} and pore volume correspond to a larger number of surface active sites and make reactant transport easier, enhancing the photocatalytic performance. The BC1I2-7-110-12 and BC2I1-4-110-12 samples possessed larger S_{BET} and pore volumes. Thus, the large S_{BET} and pore volume of BiO_xCl_y/BiO_mBr_n might be responsible for the high photocatalytic activity of the composite. The nanosheet structure can provide efficient transport paths for reactants and more active sites for photocatalytic reactions. The structure is also favorable for efficient

Table 4
Specific BET surface areas and pore parameters of the as-prepared BiO_xCl_y/BiO_mI_n samples.

Catalyst code	BET (m^2/g)	Pore size (Å)	Pore volume (cm^3/g)
BC1I2-1-160-12	7.14	429.3	0.094
BC1I2-4-160-12	11.21	357.7	0.122
BC1I2-7-160-12	15.97	479.5	0.235
BC1I2-10-160-12	3.48	445.5	0.034
BC1I2-13-160-12	0.54	777.5	0.007
BC2I1-1-160-12	8.80	461.8	0.081
BC2I1-4-160-12	16.68	382.4	0.131
BC2I1-7-160-12	10.83	510.8	0.214
BC2I1-10-160-12	3.11	432.1	0.068
BC2I1-13-160-12	1.95	632.7	0.019
BC3-1-160-12	5.13	547.1	0.053
BI3-1-160-12	2.10	423.7	0.019

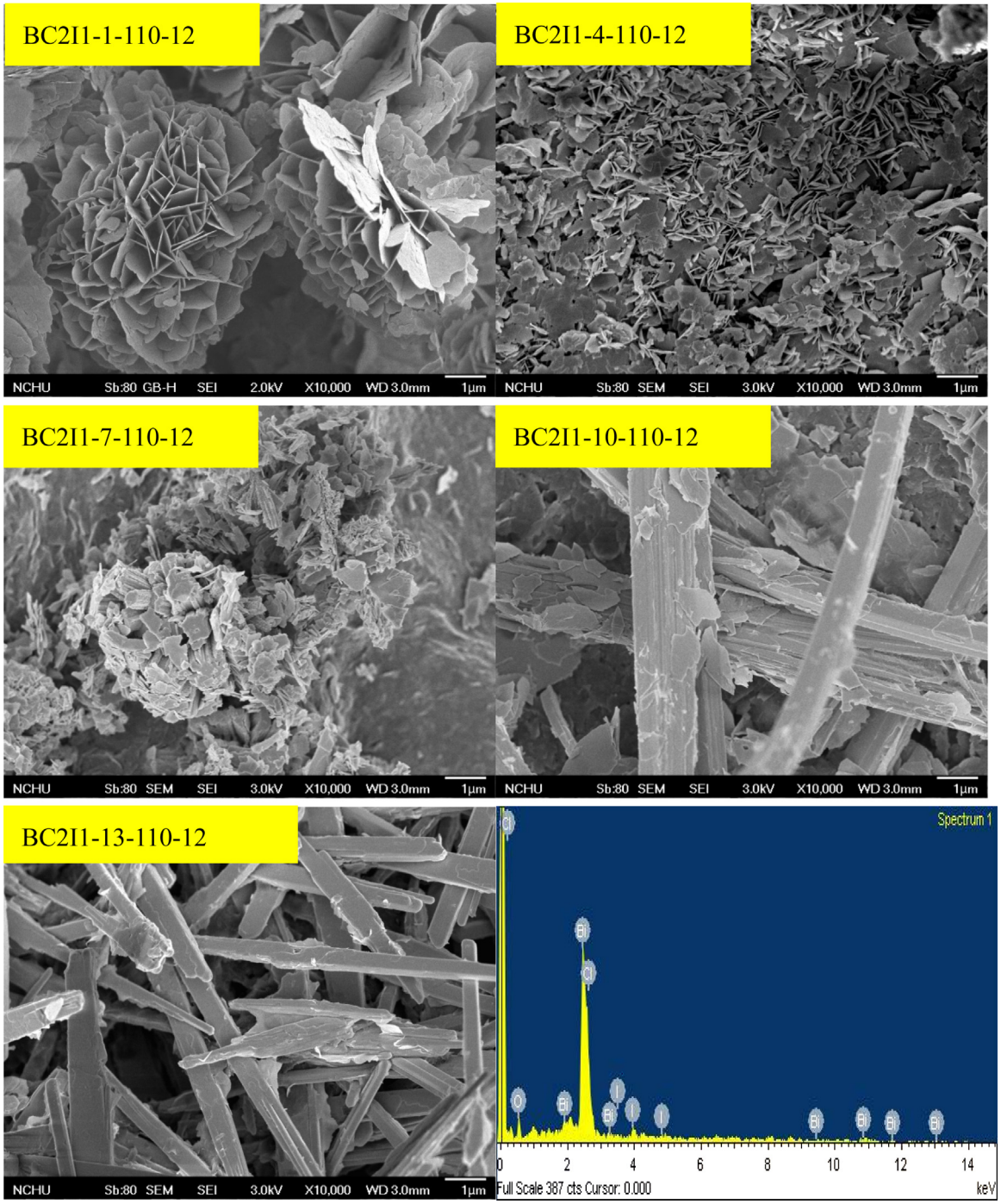

Fig. 8. SEM images of BiO_xCl_y/BiO_mI_n prepared using the autoclave hydrothermal method at various pH values (KBr/KI molar ratio = 2/1; hydrothermal conditions: temp = 110 °C; pH = 1–13; time = 12 h).

photoenergy harvesting and separating electron–hole pairs, thus enhancing photocatalytic activity.

3.2. Photocatalytic activity

The changes in the UV–vis spectra during the photodegradation of CV and phenol in aqueous dispersions of BiO_xCl_y/BiO_mI_n under visible light irradiation are illustrated in Fig. 12. After visible light irradiation for 12 h, approximately 99.5% of the CV decomposed; after UV irradiation for 36 h, nearly 99.9% of the phenol degraded. During visible light irradiation, the characteristic absorption band of the CV dye at approximately 588.3 nm decreased rapidly with slight hypochromic shifts (555.3 nm); however, no new absorption band appeared even in the ultraviolet range ($\lambda > 200$ nm), indicating the possible formation of a series of *N*-demethylated intermediates and the possible cleavage of the whole conjugated chromophore structure of the CV dye. Further irradiation caused the absorption band at 555.3 nm to decrease; however, no further wavelength shift was observed, suggesting that the band at 555.3 nm was that of the full *N*-demethylated product of the CV dye [24–26].

In Fig. 13, the degradation efficiency is shown as a function of the reaction time; the removal efficiency was substantially enhanced in the presence of BiO_xCl_y/BiO_mI_n. After irradiation for 48 h, BiO_xCl_y/BiO_mI_n exhibited superior photocatalytic

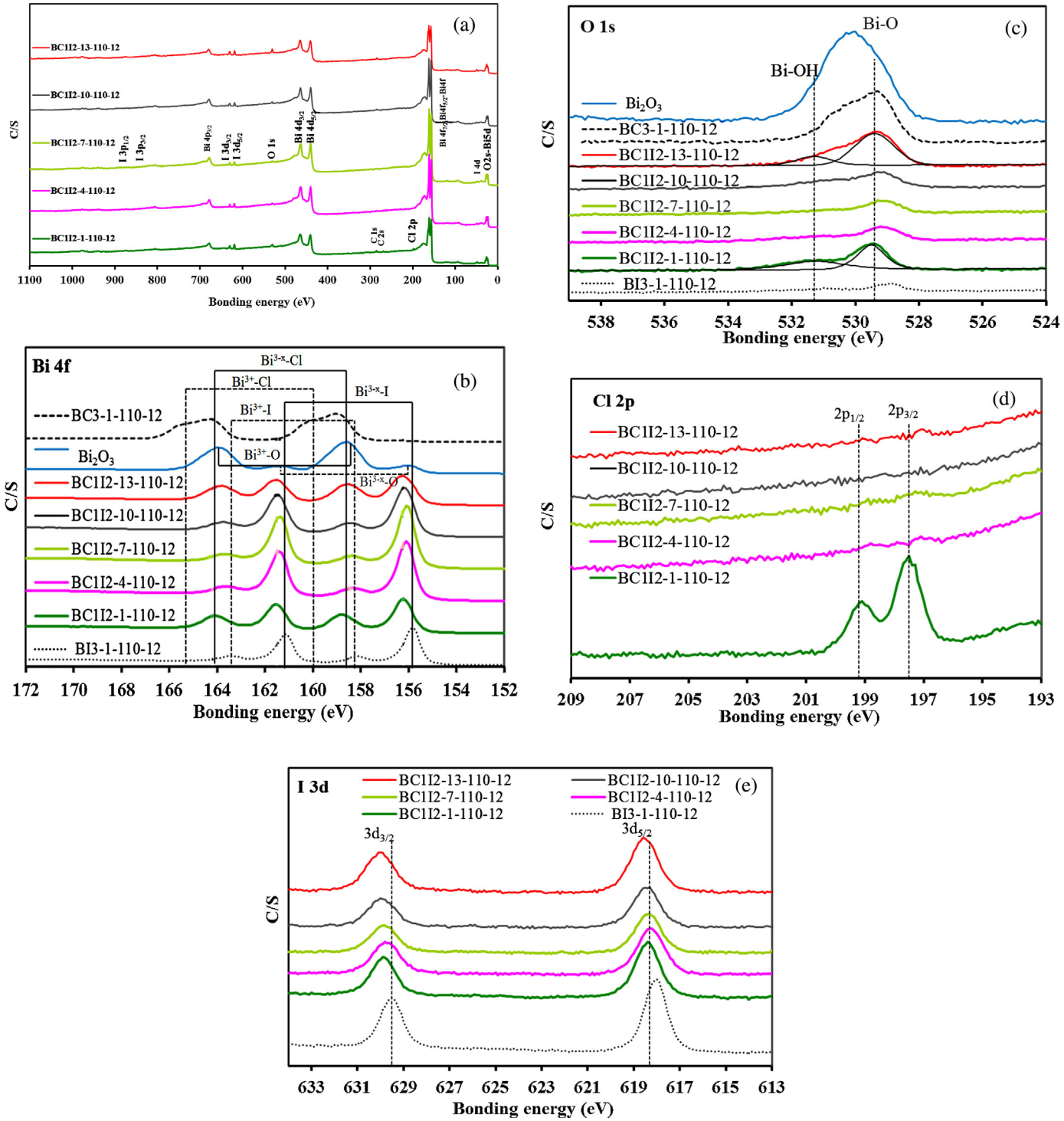

Fig. 9. High-resolution XPS spectra of as-prepared BiO_xCl_y/BiO_mI_n samples at various pH values. (a) total survey; (b) Bi 4f; (c) O 1s; (d) Cl 2p; (e) I 3d (KCl/KI molar ratio = 1/2).

performance, with a CV removal efficiency of up to 99%. To understand the reaction kinetics of CV degradation further, the apparent pseudo-first-order model [27] expressed in the equation $\ln(C_0/C) = kt$ was used in our experiments. By using the first-order linear fit of the data from Fig. 13 (Table 5), the k value of BC1I2-4-160-12 was obtained as the maximum degradation rate of $4.988 \times 10^{-1}\ h^{-1}$ by using the first-order linear fit of the data, and this value was considerably higher than that of the other composites. The $BiOCl/Bi_3O_4Cl/BiOI$ composite was a much more effective photocatalyst than the other composites synthesized in this study. The BC1I2-4-160-12 composite had a larger S_{BET} and pore volume (Table 4). However, Table 4 shows that this sample, which showed the highest S_{BET}, did not exhibit the highest photocatalytic activity among all the samples, suggesting that changes in the photocatalytic activity were associated with both the S_{BET} and BiO_xCl_y/BiO_mI_n composites. Therefore, the $BiOCl/Bi_3O_4Cl/BiOI$ composite showed the highest photocatalytic activity. Thus, the BiO_xCl_y/BiO_mI_n composites (or heterojunctions) might also play a role in enhancing the photocatalytic activity. The enhanced photocatalytic activities of BiO_xCl_y/BiO_mI_n materials could be ascribed

Table 5
The pseudo-first-order rate constants for the degradation of CV with BiO_xCl_y/BiO_mI_n photocatalysts under visible light irradiation.

pH	T (°C)							
	110 °C		160 °C		210 °C		260 °C	
	k (h^{-1})	R^2	k (h^{-1})	R^2	k (h^{-1})	R^2	k (h^{-1})	R^2
BC1I2 series								
1	0.0629	0.9646	0.1169	0.9519	0.0597	0.9550	0.1085	0.9537
4	0.1210	0.9582	0.4988	0.9698	0.3493	0.9634	0.1741	0.9561
7	0.1669	0.9599	0.1728	0.9588	0.0893	0.9689	0.1484	0.9502
10	0.0755	0.9504	0.1217	0.9572	0.1064	0.9617	0.0999	0.9568
13	0.0133	0.9585	0.0354	0.9541	0.0297	0.9663	0.0594	0.9860
BC2I1 series								
1	0.0528	0.9695	0.0318	0.9852	0.0437	0.9643	0.0227	0.9581
4	0.1939	0.9522	0.1557	0.9954	0.0931	0.9944	0.0813	0.9835
7	0.0902	0.9656	0.1604	0.9619	0.2331	0.9647	0.0833	0.9932
10	0.0737	0.9564	0.1242	0.9532	0.1030	0.9505	0.0417	0.9507
13	0.0514	0.9556	0.0502	0.9529	0.0033	0.9741	0.0355	0.9534

TiO_2 visible light irradiation	
k (h^{-1})	R^2
0.0556	0.9907

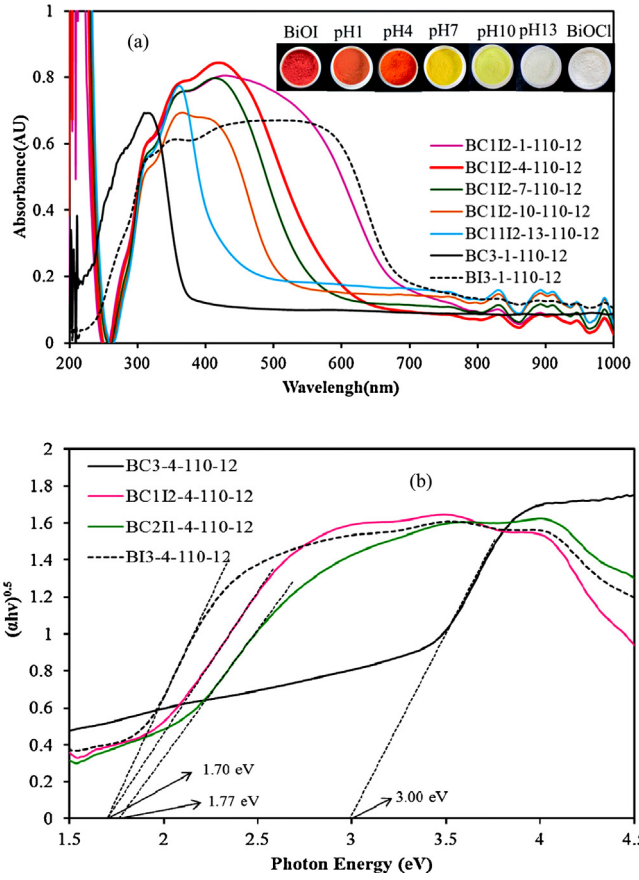

Fig. 10. UV–vis absorption spectra of as-prepared BiO_xCl_y/BiO_mI_n samples at various (a) pH values and (b) molar ratios.

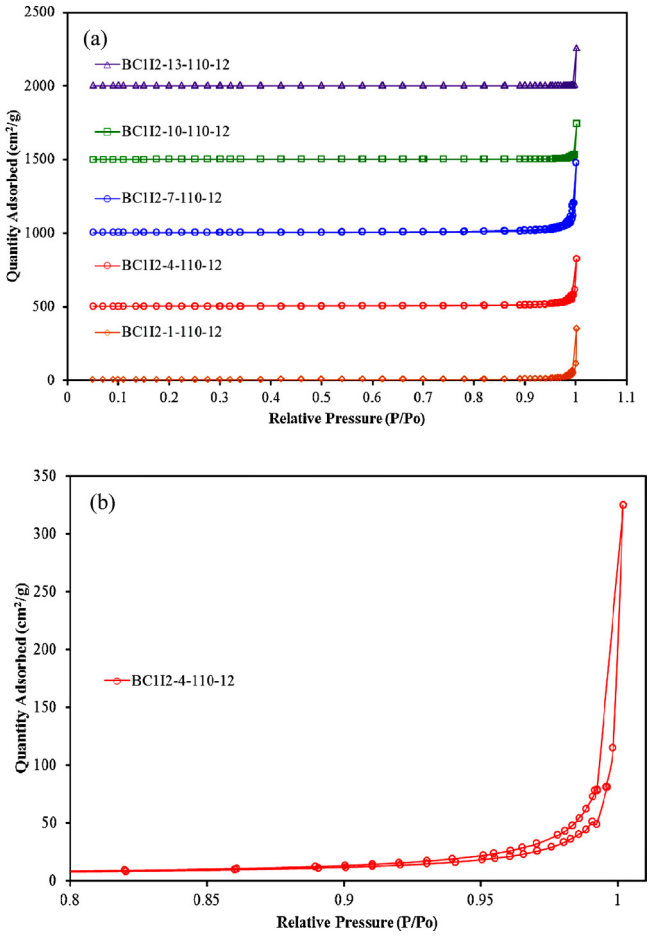

Fig. 11. N_2 adsorption–desorption isotherm distribution curves for (a) as-prepared BiO_xCl_y/BiO_mI_n samples at various pH values. (b) Enlarged view of BC1I2-4-110-12.

to the synergistic effect of the high BET surface area, formation of heterojunctions, layered structure, and low-energy band structure. In the absence of photocatalysts, CV could not be degraded under visible light irradiation; the superior photocatalytic activity of BiO_xCl_y/BiO_mI_n can be ascribed to its efficient use of visible light and the highly effective separation of electron–hole pairs within its composites.

The durability of the BC1I2-4-160-12 composite was evaluated by recycling the used catalyst. After each cycle, the catalyst was collected by centrifugation. No apparent loss was observed in the photocatalytic activity when CV were removed in the fifth cycle; even during the tenth run, the decrease in the photocatalytic activity was 1% (Fig. 14(a)). The used BC1I2-4-160-12 was also examined using XRD and no detectable difference was observed between the as-prepared and used

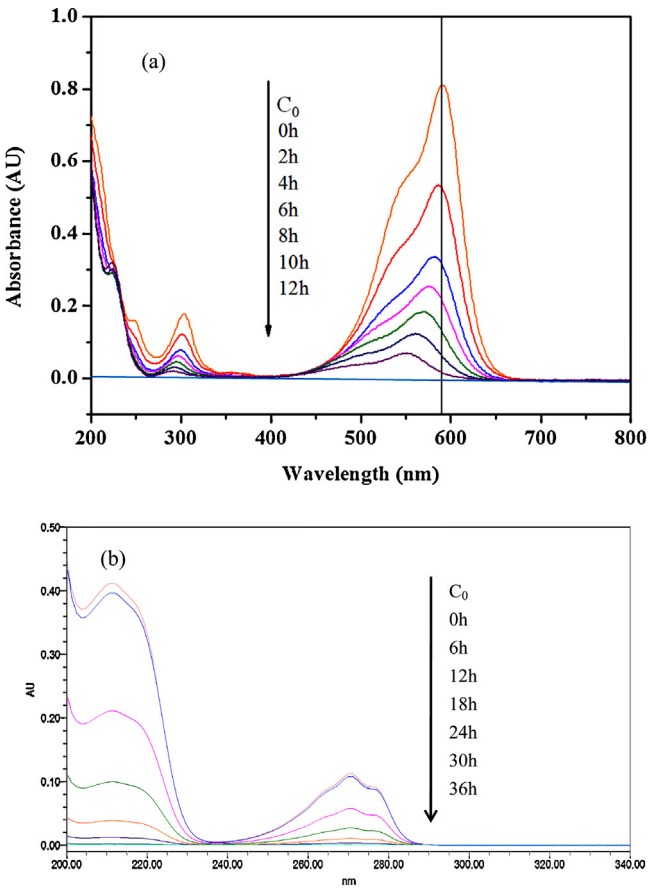

Fig. 12. Temporal UV–vis adsorption spectral changes during the photocatalytic degradation of (a) CV and (b) phenol over aqueous BB1I2-4-110-12 under visible light irradiation.

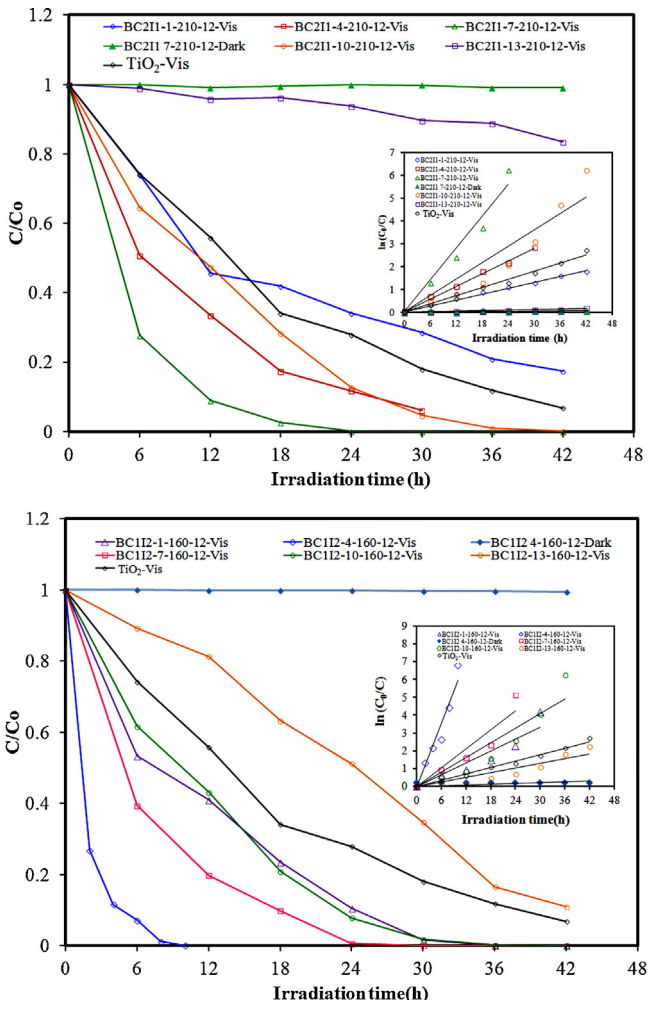

Fig. 13. Photodegradation of CV as a function of the irradiation time over various BiO_xCl_y/BiO_mI_n photocatalysts (KCl/KI molar ratio: (a) 1/2 and (b) 2/1).

samples (Fig. 14(b)); thus, the $BiOCl/Bi_3O_4Cl/BiOI$ composite has high photostability.

3.3. Photodegradation of CV

3.3.1. Separation and identification of intermediates

During visible light irradiation, temporal variations in the CV dye solution in the degradation process were examined using HPLC-PDA-ESI-MS. In the course of irradiating CV solutions for up to 24 h at pH 4, chromatograms were recorded at 580, 350, and 300 nm (Fig. 15); 19 intermediates were identified to have retention times shorter than 50 min. The CV dye and its related intermediates were denoted as species A–J, a–f, and α–γ. Except for the initial CV dye (Peak A), the peaks initially increased and then decreased, indicating the formation and transformation of the intermediate compounds.

The maximum absorption of the spectral bands shifted from 585.5 nm (Spectrum A) to 543.8 nm (Spectrum J), from 377.1 nm (Spectrum a) to 342.6 nm (Spectrum f), and from 288.3 nm (Spectrum α) to 274.8 nm (Spectrum γ) (Table 6 and Fig. S12). They were identified as A–J, a–f, and α-γ, respectively, and they corresponded to Peaks A–J, a–f, and α–γ (Fig. 15). These shifts of the absorption bands were presumed to result from the formation of a series of *N*-demethylated intermediates. From the results obtained, several classes of intermediates could be distinguished. The details of the separation and identification of intermediates have been provided in Figs. S12 and S13 of supplementary materials.

3.4. Photodegradation mechanisms of CV

Three possible reaction mechanisms have been proposed for dye photodegradation using a semiconductor: (1) photolysis, (2) dye photosensitization, and (3) photocatalysis [28]. In the photolysis process, a photoinduced electron on the induced dye directly reacts with O_2 to produce a singlet oxygen atom that acts as an oxidant for the pure dye's photolysis [28,29]. In our experiments, CV degradation by photolysis under visible light was not observable in a blank experiment; CV has a stable structure, and decomposition by photolysis was negligible.

In the dye photosensitization process, the energy of the irradiating light can stimulate the dye to form photoinduced electrons that are transferred to the conduction band of the catalyst that absorbs the dye. Subsequently, the transferred electrons react with O_2 to generate the oxidant $O_2^{\bullet-}$ [21,28]. In this study, slight changes in the CV concentration between various samples could be detected within 30 min of the dark adsorption experiments, that is, before the photocatalytic reactions began. The slight CV adsorption on the catalyst is beneficial for the transfer of charge carriers between the dye and the catalyst surfaces in the dye photosensitization process. Presumably, photosensitization processes can proceed in the presence of BiO_xCl_y/BiO_mI_n; in other words, the possibility of the photosensitization mechanism playing a role in CV decomposition cannot be ruled out.

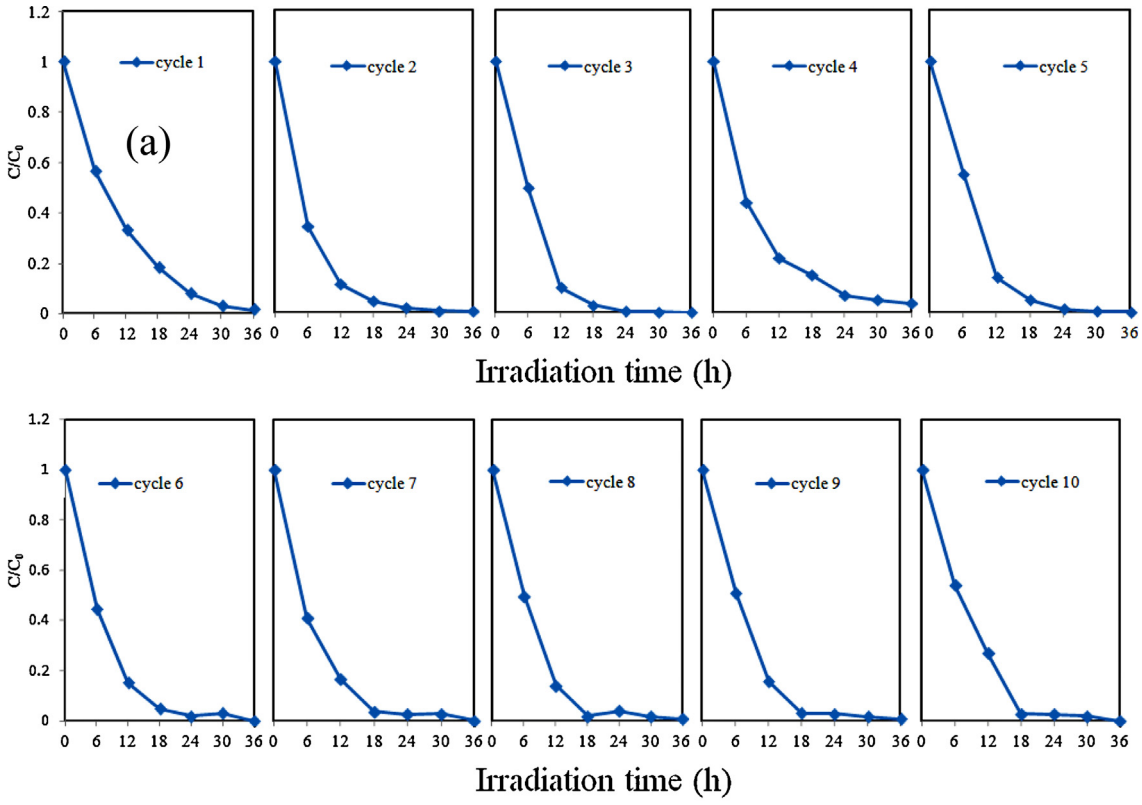

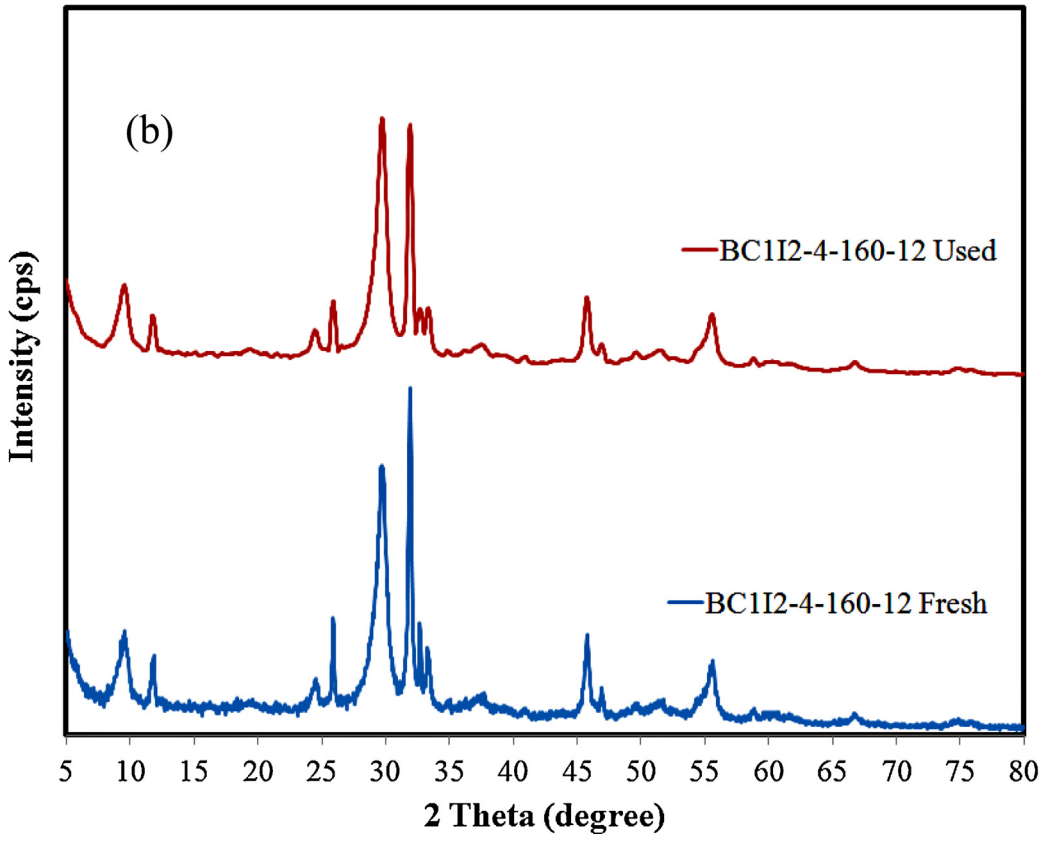

Fig. 14. (a) Cycling runs and (b) XRD patterns acquired before and after the photocatalytic degradation of CV in the presence of BC1I2-4-160-12.

Table 6
Intermediates of the photocatalytic degradation of CV identified by HPLC-ESI-MS. Conditions: BiO_xCl_y/BiO_mI_n, 10 mg L^{-1} CV, irradiation 24-h.

HPLC peaks	Intermediates	ESI-MS spectrum ions (*m*/*z*)	Absorption maximum (nm)
A	*N*,*N*,*N*′,*N*′,*N*″,*N*″-hexaethyl pararosaniline	372.23	588.4
B	*N*,*N*-dimethyl-*N*′,*N*′-dimethyl-*N*″-methyl pararosaniline	358.18	581.2
C	*N*,*N*-dimethyl-*N*′-methyl-*N*″-methylpararosaniline	344.18	573.9
D	*N*,*N*-dimethyl-*N*′,*N*′-dimethyl pararosaniline	344.16	584.9
E	*N*-methyl-*N*′-methyl-*N*″-methyl pararosaniline	330.12	566.5
F	*N*,*N*-dimethyl-*N*′-methylpararosaniline	330.14	570.2
G	*N*-methyl-*N*′-methyl pararosaniline	316.12	562.9
H	*N*,*N*-dimethyl pararosaniline	316.13	563.7
I	*N*-methyl pararosaniline	302.12	555.5
J	Pararosaniline	288.07	543.8
a	4-(*N*,*N*-dimethylamino)-4′-(*N*′,*N*′-dimethylamino)benzophenone	268.97	376.8
b	4-(*N*,*N*-dimethylamino)-4′-(*N*′-methylamino)benzophenone	255.11	366.2
c	4-(*N*-methylamino)-4′-(*N*′-methylamino)benzophenone	241.11	362.8
d	4-(*N*,*N*-dimethylamino)-4′-aminobenzophenone	241.08	364.6
e	4-(*N*-methylamino)-4′-aminobenzophenone	227.05	357.0
f	4,4′-Bis-aminobenzophenone	213.03	342.3
α	4-(*N*,*N*-dimethylamino)phenol	138.05	287.9
β	4-(*N*-methylamino)phenol	N/A	286.3
γ	4-Aminophenol	N/A	274.3

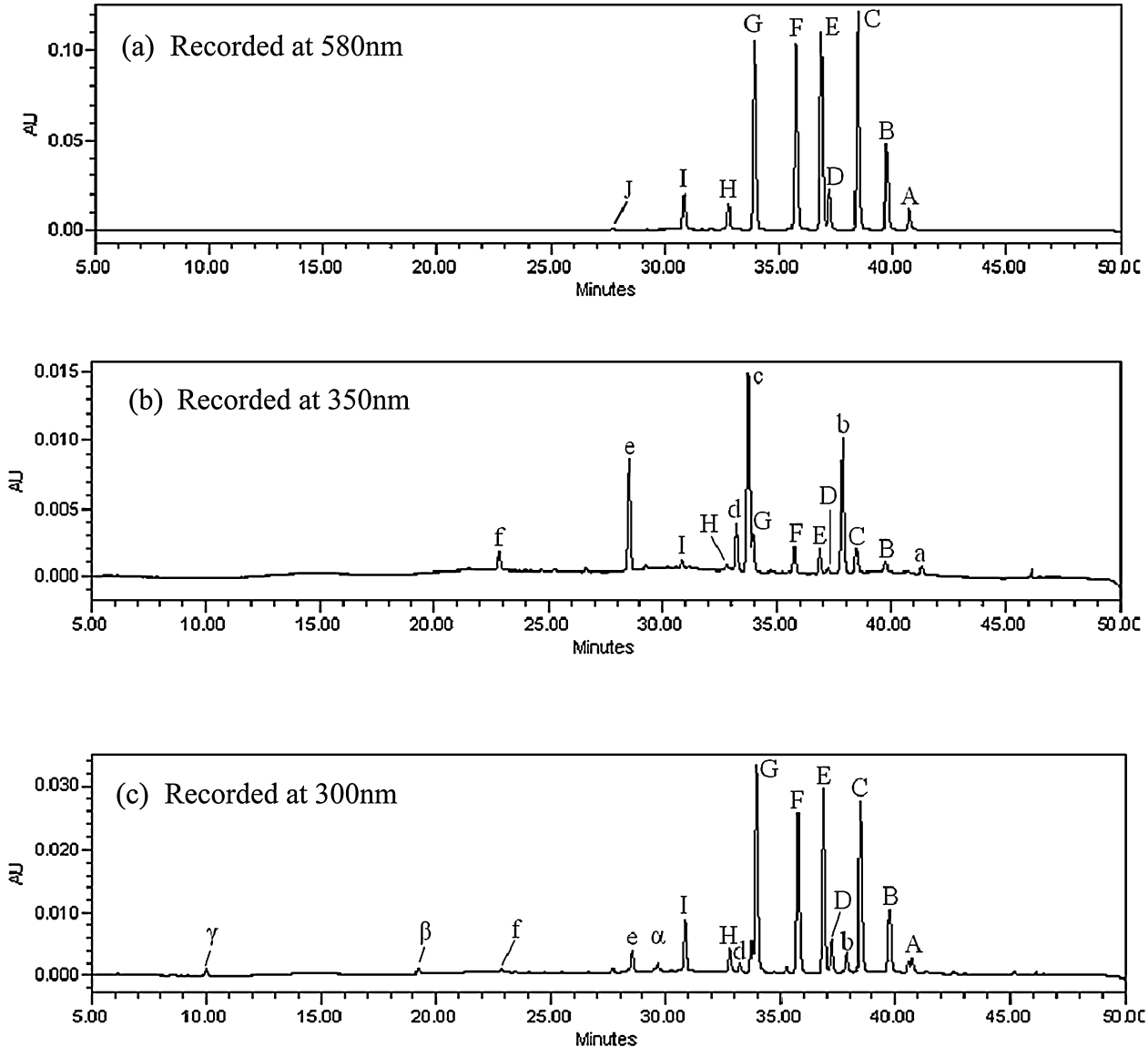

Fig. 15. HPLC chromatogram of the degraded intermediates at various irradiation intervals, recorded at (a) 580 nm (b) 350 nm, and (c) 300 nm.

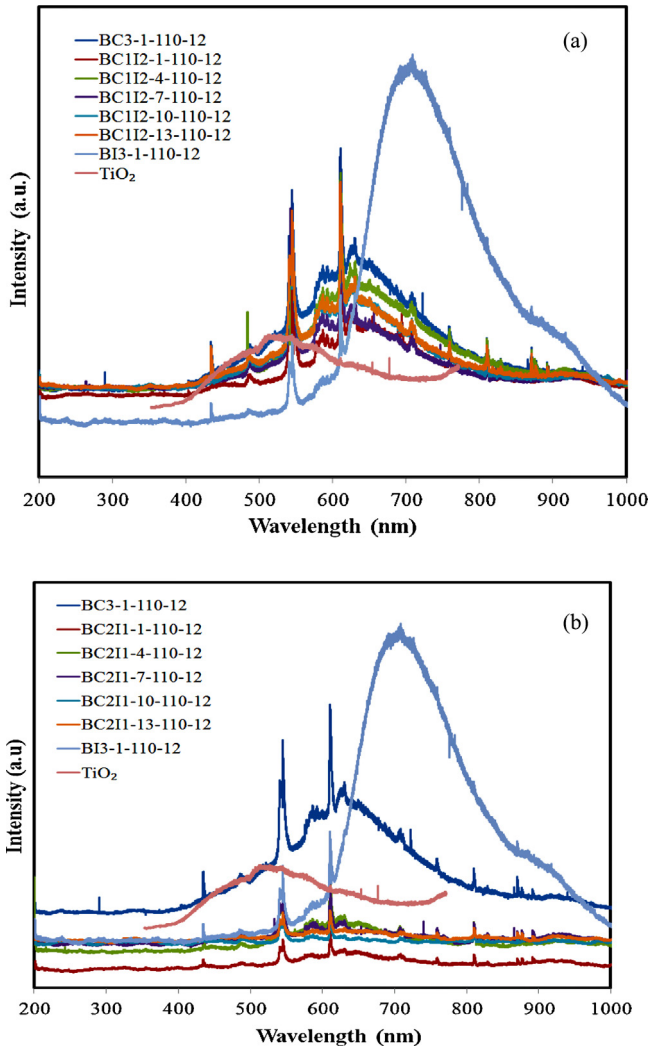

Fig. 16. Photoluminescence spectra of TiO_2, BiOCl, BiOI, and BiO_xCl_y/BiO_mI_n (KCl/KI molar ratio: (a) 1/2 and (b) 2/1).

The CL spectra were used to investigate the recombination rate of the photogenerated electron–hole pairs [30]. To investigate the separation capacity of the photogenerated carriers in the heterostructures, the CL spectra of BiOCl, BiOI, and BiO_xCl_y/BiO_mI_n were measured; the results are shown in Fig. 16. A strong emission peak appeared at approximately 2.01 and 1.85 eV for BiOCl (BC3-1-110-12) and BiOI (BB3-1-110-12), and it might have been derived from the direct electron–hole recombination of band transitions. However, the characteristic emission peak at approximately 2.01 eV nearly disappeared for BiO_xCl_y/BiO_mI_n, indicating that the recombination of photogenerated charge carriers was greatly inhibited. The efficient separation of charge might increase the lifetime of charge carriers and enhance the efficiency of interfacial charge transfer to the adsorbed substrates, thus improving the photocatalytic activity [12,31,32]. The low relative CL intensities of BC1I2-7-110-12 and BC2I1-110-4-12 composites, as shown in Fig. 16(a) and (b), suggest that they possess the lowest recombination rate of electron–hole pairs, resulting in their higher photocatalytic activity, as shown in Fig. 13(a) and (b) and Table 5. Therefore, we suggest that the CV degradation is initiated not only by photocatalysis but also by photosensitization.

Various primary reactive species, such as HO•, h^+, $O_2^{\bullet-}$, H•, and $^1O_2$, could be formed during photocatalytic degradation processes in UV–vis/semiconductor systems [14,32,33]. Chen et al. proposed a pathway for generating active oxygen radicals (OH•) on the surface of $Bi_2O_2CO_3$/BiOI for the degradation of methylene blue, rhodamine-B, and CV [34]. Xiao et al. revealed that high-efficiency visible-light-driven bisphenol-A removal with BiOI/BiOCl could be attributed to effective separation and transfer of photoinduced charge carriers in BiOI/BiOCl, leading to a narrower bandgap and more negative conduction band position. The narrow bandgap and negative conduction band position favored the photogenerated holes [35]. Shenawi-Khalil et al. showed that rhodamine-B photodegradation by $yBiO(Cl_xBr_{1-x})$–$(1-y)$ bismuth oxide hydrate under visible light was dominated by $O_2^{\bullet-}$ and h^+ oxidation being the main active species [36]. Cao et al. observed that hydroxyl radicals and direct holes were the primary reactive species in methyl orange degradation by BiOI/BiOBr spheres under visible light irradiation [21]. Sanaa et al. reported that OH• and h^+ were the two main actives in the entire degradation process [37]. Wang et al. reported that the OH• radical was generated through multistep reduction $O_2^{\bullet-}$ [10]. The generation of $O_2^{\bullet-}$ could not only inhibit the recombination of photoinduced charge carriers, but also benefit the dechlorination of a chlorinated phenol derivative. The hydroxyl radical HO• might be generated only through the $e^- \rightarrow O_2^{\bullet-} \rightarrow H_2O_2 \rightarrow OH^{\bullet}$ route. Furthermore, the OH• radical was generated through multistep reduction $O_2^{\bullet-}$ in the system. In a valence band of Bi^{3+}, holes formed through photoexcitation were regarded as Bi^{5+} [38]. The standard redox potential of Bi^{5+}/Bi^{3+} was more negative than that of $OH^{\bullet}/OH^-$ [39]. Therefore, photogenerated holes on the surface of bismuth oxyhalides were not expected to react with OH^-/H_2O to form OH•, suggesting that the decomposition of bisphenol-A [35] and rhodamine [36] could be attributed to a direct reaction with the photogenerated holes or with a superoxide radical (generated by the excited electron) or with both species. Zhu et al. reported that photocatalytic experiments in the presence of N_2 and a radical scavenger suggested that OH• and $O_2^{\bullet-}$ were the two main actives in the entire degradation process [40]. Dimitrijevic et al. [33] proposed that the water dissociated on the surface of TiO_2 and in subsequent molecular layers had three roles: (1) stabilizing charges (preventing electron–hole recombination), (2) acting as an electron donor (reaction of water with photogenerated holes to generate OH• radicals), and (3) acting as an electron acceptor (formation of H atoms in a reaction of photogenerated electrons with protons on the surface, $-OH_2^+$). According to previous studies [41], the dominant active oxygen species generated in direct oxidation and photocatalytic reactions are $^1O_2$ and OH• radicals, respectively. Moreover, in this visible light-induced semiconductor system, hydroxylated compounds were also identified for the photocatalytic degradation of CV and ethyl violet [42]. Based on the aforementioned studies, we proposed that the probability of forming OH• should be much lower than that of forming $O_2^{\bullet-}$; however, OH• is an extremely strong, nonselective oxidant that leads to the partial or complete mineralization of several organic chemicals.

To evaluate the effect of the active species during the photocatalytic reaction, a series of quenchers were introduced to scavenge the relevant active species. OH•, $O_2^{\bullet-}$, $^1O_2$, and h^+ were investigated by adding 1.0 mM benzoquinone (BQ, a quencher of $O_2^{\bullet-}$) [43], 1.0 mM isopropanol (IPA, a quencher of OH•) [44], 1.0 mM ammonium oxalate (AO, a quencher of h^+) [45], and 1.0 mM sodium azide (SA), a quencher of $^1O_2$ [46], respectively. The method is similar to the photocatalytic activity test. As shown in Fig. 17, the degradation efficiency of IPA quenching decreased more than that of AO, and the degradation efficiency of BQ quenching decreased more than that of IPA, but the photocatalytic degradation of CV was not affected by the addition of SA. In short, the quenching effects of various scavengers showed that the reactive $O_2^{\bullet-}$ played a major role, and OH• or h^+ played a minor role in CV degradation.

Fan et al. reported [47] that Pt-TiO_2 accumulated less negative species on catalyst surfaces, which reduced reaction rates,

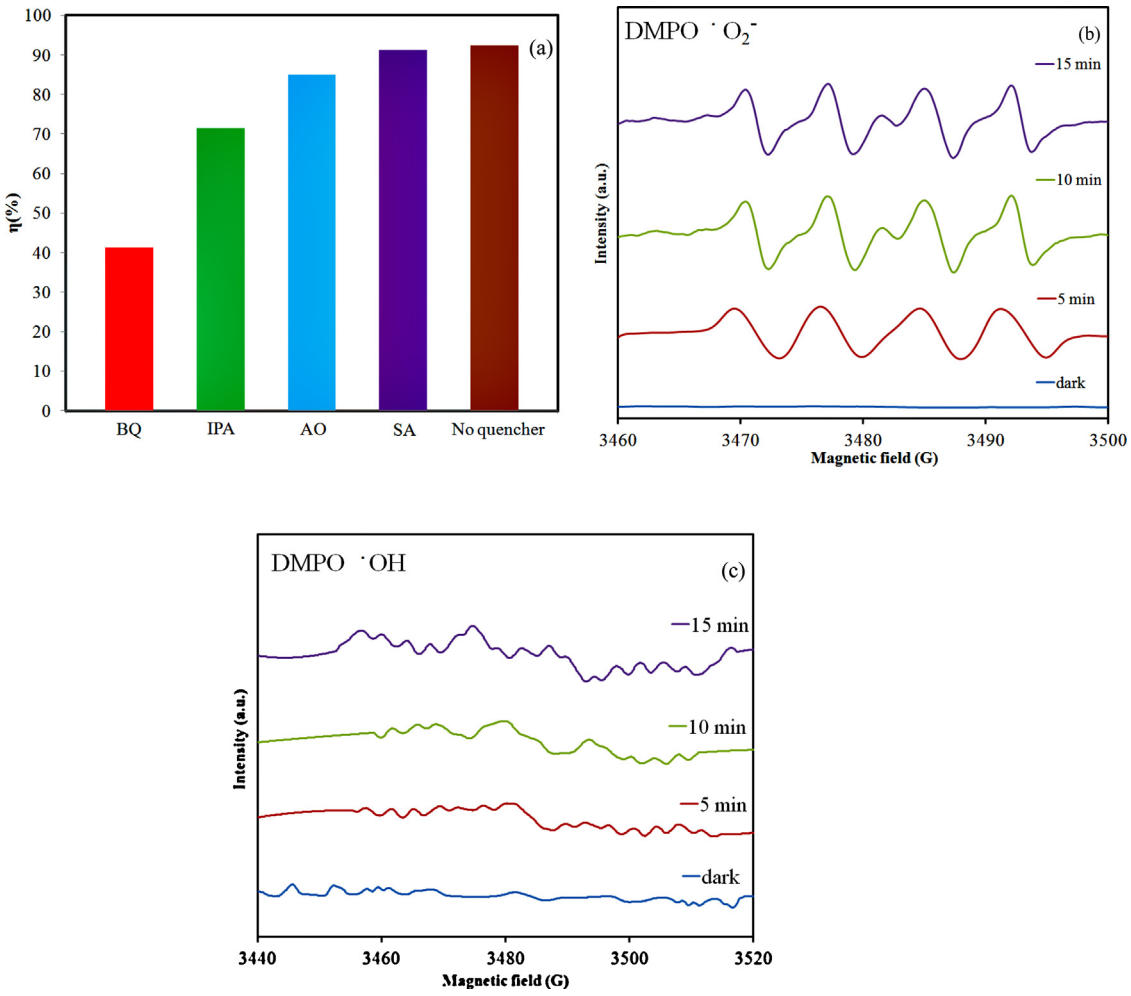

Fig. 17. (a) The dye concentration during photodegradation as a function of irradiation time observed in BiO_xCl_y/BiO_mI_n under the addition of different scavengers: SA, IPA, AQ, and BQ; (b and c) DMPO spin-trapping EPR spectra for DMPO-O_2^- and DMPO-OH under visible light irradiation with BiO_xCl_y/BiO_mI_n.

compared with pure TiO_2 in an acidic environment. The OH• radical was produced subsequently, as shown in Eqs. (18)–(23):

$$O_2^{\bullet-} + H^+ + e^- \rightarrow HOO^\bullet \quad (18)$$

$$HOO^\bullet + H_2O \rightarrow OH^\bullet + H_2O_2 \quad (19)$$

$$O_2^{\bullet-} + 2H^+ \rightarrow H_2O_2 \quad (20)$$

$$H_2O_2 + e^- \rightarrow OH^\bullet + OH^- \quad (21)$$

$$h^+ + OH^- \rightarrow OH^\bullet \quad (22)$$

$$h^+ + H_2O \rightarrow OH^\bullet + H^+ \quad (23)$$

These cycles continuously occur when the system is exposed to visible light irradiation [47]; after several cycles of photooxidation, the degradation of CV by the formed oxidant species can be expressed using Eqs. (24)–(26):

$$CV + h^+ \rightarrow CV^{\bullet+} \rightarrow \text{degradedcompounds} \quad (24)$$

$$CV + OH^\bullet/O_2^{\bullet-} \rightarrow \text{degradedcompounds} \quad (25)$$

$$CV^{\bullet+} + OH^\bullet/O_2^{\bullet-} \rightarrow \text{degradedcompounds} \quad (26)$$

The dye exhibited a dye-sensitized degradation mechanism [40,48]. The photocatalytic degradation can also be attributed to the photodegradation of CV through the photocatalytic pathway of CV-photosensitized BiO_xCl_y/BiO_mI_n. When a visible photon is absorbed, CV is promoted to an excited electronic state, CV*, from which an electron can be transferred into the conduction band of BiO_xCl_y/BiO_mI_n:

$$CV + h\nu \rightarrow CV* \quad (27)$$

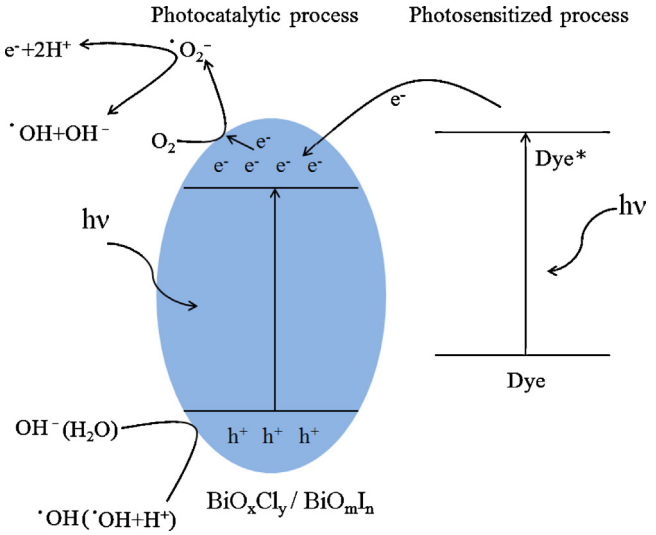

Fig. 18. The band structure diagram of BiO_xCl_y/BiO_mI_n nanocomposites and possible charge separation processes.

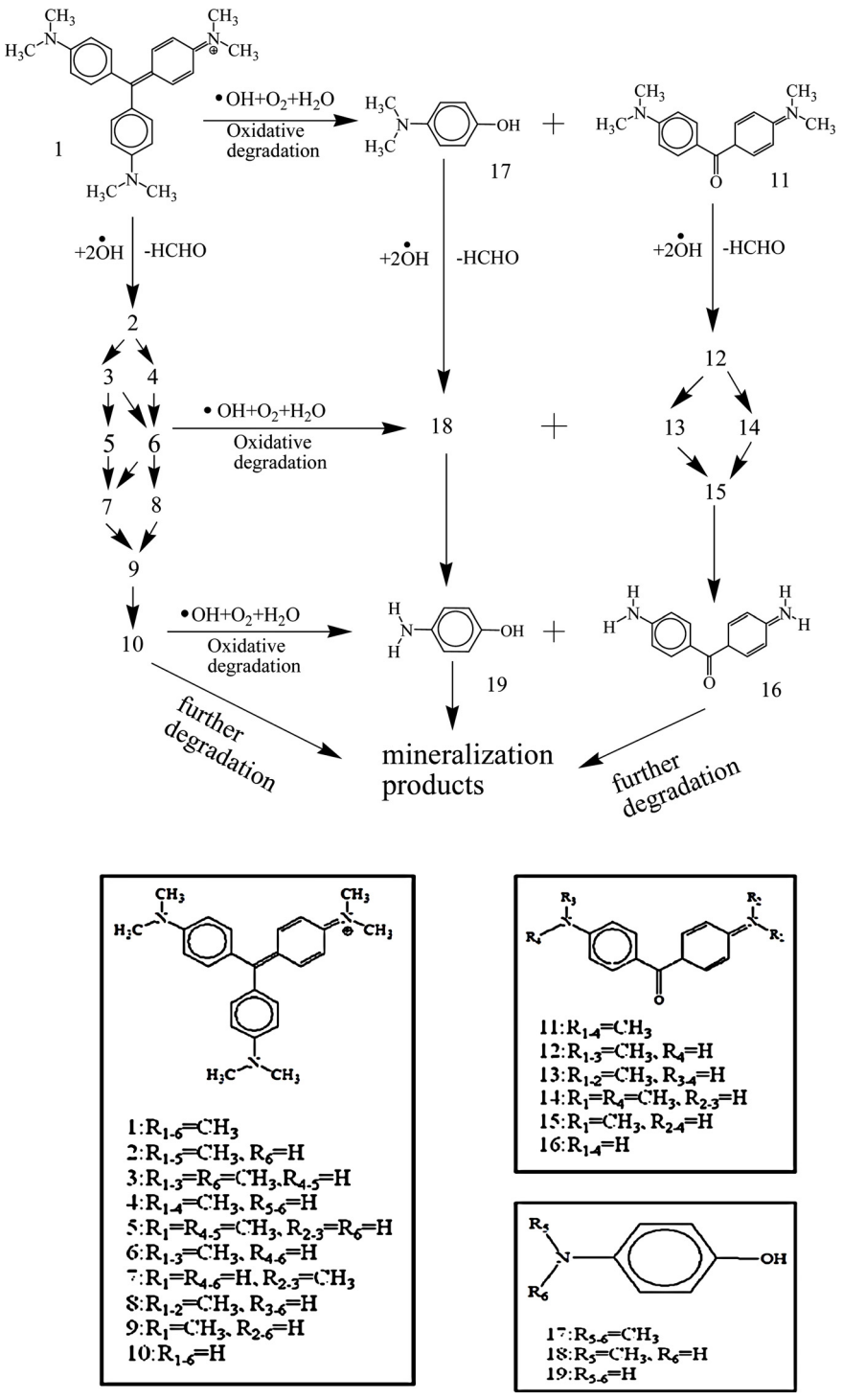

Fig. 19. Proposed photodegradation mechanism for the CV dye.

$$CV* + BiO_xCl_y/BiO_mI_n \rightarrow CV^{\bullet+} + BiO_xCl_y/BiO_mI_n(e^-) \quad (28)$$

$$O_2 + e^- \rightarrow O_2^{\bullet-} \quad (29)$$

Once the electron reaches the BiO_xCl_y/BiO_mI_n conduction band, it induces the generation of active oxygen species, which cause the degradation of CV. It is clear that, apart from the photodegradation of CV through the pathway of BiO_xCl_y/BiO_mI_n-mediated and photosensitized processes, another type of photocatalytic pathway accounts for the enhanced photocatalytic activity. Both the photocatalytic and photosensitized processes proceed concurrently (Fig. 18). However, in photocatalytic and photosensitized reaction conditions, $O_2^{\bullet-}$ are formed by the reaction of photogenerated and photosensitized e^- with O_2 on the photocatalyst surface, and $OH^\bullet$ radical is also formed by the reaction of $O_2^{\bullet-}$ with H^+ and h^+ with OH^- (or H_2O). The $OH^\bullet$ radical is produced subsequently, as shown in Eqs. (18)–(23) [38]. Fig. 17a indicates that $^1O_2$ can be negligible, whereas $O_2^{\bullet-}$ is a major active species and $OH^\bullet$ and h^+ are minor active species in the process of CV degradation. What's more, dissolved oxygen might trap the photogenerated electrons to from $O_2^{\bullet-}$, which is beneficial to promote the decomposition of CV. This photocatalytic mechanism is consistent with the above analysis of the band structure of BiO_xCl_y/BiO_mI_n, and may be further confirmed

using EPR technique [49]. Fig. 17 indicated that no EPR signals were observed when the reaction was performed in the dark, while the signals with intensity of corresponding to the characteristic peak of DMPO-O_2^- (Fig. 17b) and DMPO-OH (Fig. 17c) adducts were observed during the reaction process under visible light irradiation, and the intensity gradually increased with the prolonged reaction time, suggesting that the $O_2^{\bullet-}$ (major active species) and the $OH^\bullet$ (minor active species) has been formed in presence of BiO_xCl_y/BiO_mI_n and oxygen under visible light irradiation.

In earlier reports [8,9,47], the *N*-dealkylation processes were preceded by the formation of a nitrogen-centered radical, and the oxidative degradation (destruction of the dye chromophore structure) was preceded by the generation of a carbon-centered radical in the photocatalytic degradation of triphenylmethane dye. On the basis of the aforementioned experimental results, a dye degradation mechanism was tentatively proposed (Fig. 19). The excited dye injects an electron into the conduction band of bismuth oxybromide, where it is scavenged by O_2 to form $O_2^{\bullet-}$. Demethylation of CV dye occurs mostly through attack by the active species, which is a perfect nucleophilic reagent, on the *N*-methyl portion of CV. $O_2^{\bullet-}$ subsequently reacts with H_2O to generate $OH^\bullet$ radical and another active radical. The probability of $^\bullet OH$ formation should be much lower than that of $O_2^{\bullet-}$ formation. $OH^\bullet$ is an extremely strong, nonselective oxidant that leads to the partial or complete mineralization of several organic chemicals. All the aforementioned active radicals drive the photodegradation or mineralization of the dye molecule. Under visible light irradiation, all the intermediates identified in these two topics have the same result. The major oxidant is clearly the $OH^\bullet$ radical, not $O_2^{\bullet-}$.

During the initial period of CV dye photodegradation by bismuth oxybromide, competitive reactions between *N*-demethylation and oxidative degradation (cleavage of the CV chromophore ring structure) occurred, and the reactions involved the intermediates identified. The detailed mechanisms are illustrated in Figs. S14–S15. The first pathway involves a hydroxyl radical attack on the *N*,*N*-methylamino group of CV, resulting in the formation of a reactive cationic radical; the subsequent demethylation and oxidation of the cationic radical eventually yield the first group of intermediates. The results indicate that the *N*-demethylation degradation of the CV dye occurred in a stepwise manner to yield mono-, di-, tri-, tetra-, penta-, and hexa-*N*-demethylated CV species.

The second pathway involves a hydroxyl radical attack on the central carbon atom of CV, yielding a reactive cationic radical; a bond between the central carbon atom and the *N*,*N*-dimethylamino phenyl ring is cleaved to give one set of intermediates a and α. These intermediates can be further attacked by hydroxyl radicals, giving a reactive cationic radical that is demethylated and yielding f and γ. These intermediates are further oxidized to form mineralization products.

4. Conclusion

Control experiments were conducted to investigate the influence of pH on the hydrothermal reactions used in composite synthesis. The increased photocatalytic activities of BiO_xCl_y/BiO_mI_n could be attributed to the formation of a heterojunction between BiO_xCl_y and BiO_mI_n, which effectively suppressed the recombination of photoinduced electron–hole pairs. The enhanced photocatalytic activities of BiO_xCl_y/BiO_mI_n materials could be ascribed to the synergistic effect of the high BET surface area, layered structure, formation of a heterojunction, and low-energy band structure. Both the photocatalytic process and photosensitized process proceeded concurrently for CV degradation, whereas the photocatalytic process was the sole process in phenol degradation. $O_2^{\bullet-}$ was the main active species, and $OH^\bullet$ or h^+ were the minor active species in the photocatalytic process. In the photocatalytic and photosensitized processes, *N*-demethylation as well as the cleavage of the conjugated CV dye structure occurred during degradation with BiO_xCl_y/BiO_mI_n as the catalyst. The reaction mechanisms proposed in this study are expected to offer useful insights into future technological applications of the process of dye degradation by visible light.

Acknowledgments

This research was supported by the Ministry of Science and Technology of the Republic of China (NSC-101-2113-M-142-001-MY3).

Appendix A. Supplementary data

Supplementary data associated with this article can be found, in the online version, at http://dx.doi.org/10.1016/j.jhazmat.2014.10.025.

References

[1] Ullmann's Encyclopedia of Industrial, Chemistry, Part A27, Triarylmethane and Diarylmethane Dyes, 6th ed., Wiley-VCH, New York, 2001.
[2] L.M. Lewis, G.L. Indig, Effect of dye aggregation on triarylmethane-mediated photoinduced damage of hexokinase and DNA, J. Photochem. Photobiol. B: Biol. 67 (2002) 139–148.
[3] B.P. Cho, T. Yang, L.R. Blankenship, J.D. Moody, M. Churchwell, F.A. Bebland, S.J. Culp, Synthesis and characterization of *N*-demethylated metabolites of Malachite green and Leucomalachite green, Chem. Res. Toxicol. 16 (2003) 285–294.
[4] W.H. Chung, C.S. Lu, W.Y. Lin, J.X. Wang, C.W. Wu, C.C. Chen, Determining the degradation efficiency and mechanisms of ethyl violet using HPLC-PDA-ESI-MS and GC-MS, Chem. Cent. J. 6 (2012) 63.
[5] K. Yu, S. Yang, C. Liu, H. Chen, H. Li, C. Sun, S.A. Boyd, Degradation of organic dyes via bismuth silver oxide initiated direct oxidation coupled with sodium bismuthate-based visible light photocatalysis, Environ. Sci. Technol. 46 (2012) 7318–7326.
[6] W.L.W. Lee, J.S. Lin, J.L. Chang, J.Y. Chen, M.C. Cheng, C.C. Chen, Photodegradation of CV over nanocrystalline bismuth tungstate prepared by hydrothermal synthesis, J. Mol. Catal. A: Chem. 361–362 (2012) 80–90.
[7] F. Chen, P. Fang, Y. Gao, Z. Liu, Y. Liu, Y. Dai, Effective removal of high-chroma crystal violet over TiO_2-based nanosheet by adsorption-photocatalytic degradation, Chem. Eng. J. 204–206 (204) (2012) 107–110.
[8] S. Ameen, M.S. Akhtar, M. Nazim, H.S. Shin, Rapid photocatalytic degradation of crystal violet dye over ZnO flower nanomaterials, Mater. Lett. 96 (2013) 228–232.
[9] W.L.W. Lee, W.H. Chung, W.S. Huang, W.C. Lin, W.Y. Lin, Y.R. Jiang, C.C. Chen, Photocatalytic activities of nano-cubic barium titanate by hydrothermal synthesis, J. Taiwan Inst. Chem. Eng. 44 (2013) 660–669.
[10] J. Wang, Y. Yu, L. Zhang, Highly efficient photocatalytic removal of sodium pentachlorophenate with Bi_3O_4Br under visible light, Appl. Catal. B: Environ. 136–137 (2013) 112–121.
[11] L. Ye, J. Chen, L. Tian, J. Liu, T. Peng, K. Deng, L. Zan, BiOI thin film via chemical vapor transport: Photocatalytic activity, durability, selectivity and mechanism, Appl. Catal. B: Environ. 130–131 (2013) 1–7.
[12] F. Dong, Y. Sun, M. Fu, Z. Wu, S.C. Lee, Room temperature synthesis and highly enhanced visible light photocatalytic activity of porous BiOI/BiOCl composite nanoplate microflowers, J. Hazard. Mater. 219–220 (219) (2012) 26–30.
[13] E. Keller, V. Kramer, A strong deviation from Vegard's rule: X-ray powder investigations of the three quasi-binary phase systems BiOX-BiOY (X,Y = Cl,Br,I), Z. Naturforsch. B. 60 (2005) 1255–1263.
[14] X. Xiao, R. Hao, M. Liang, X. Zuo, J. Nan, L. Li, W. Zhang, One-pot solvothermal synthesis of three-dimensional (3D) BiOI/BiOCl composites with enhanced visible light photocatalytic activities for the degradation of bisphenol A, J. Hazard. Mater. 233–234 (233) (2012) 122–130.
[15] F. Dong, Y. Sun, M. Fu, Z. Wu, S.C. Lee, Room temperature synthesis and highly enhanced visible light photocatalytic activity of porous BiOI/BiOCl composites nanoplates microflowers, J. Hazar. Mater. 219–220 (2012) 26–34.
[16] X. Xiao, R. Hao, X. Zuo, J. Nan, L. Li, W. Zhang, Microwave-assisted synthesis of hierarchical $Bi_7O_9I_3$ microsheets for efficient photocatalytic degradation of bisphenol-A under visible light irradiation, Chem. Eng. J. 209 (2012) 293–300.
[17] N.M. Mahmoodi, Photocatalytic ozonation of dyes using multiwalled carbon nanotube, J. Mol. Catal. A: Chem. 366 (2013) 254–260.
[18] N.M. Mahmoodi, M. Arami, N.Y. Limaee, Photocatalytic degradation of triazinic ring-containing azo dye (Reactive Red 198) by using immobilized TiO_2 photoreactor: bench scale study, J. Hazard. Mater. 133 (2006) 113–118.
[19] K.G. Keramidas, G.P. Voutsas, P.I. Rentzeperis, The crystal structure of BiOCI, Z. Kristalogr. 205 (1993) 35–40.

[20] K.L. Zhang, C.M. Liu, F.Q. Huang, C. Zheng, W.D. Wang, Study of the electronic structure and photocatalytic activity of the BiOCl photocatalyst, Appl. Catal. B: Environ. 68 (2006) 125–129.
[21] J. Cao, B.Y. Xu, B.D. Luo, H.L. Lin, S.F. Chen, Novel BiOI/BiOBr heterojunction photocatalysts with enhanced visible light photocatalytic properties, Catal. Commun. 13 (2011) 63–68.
[22] J. Zhang, F. Shi, J. Lin, D. Chen, J. Gao, Z. Huang, X. Ding, C. Tang, Self-assembled 3-D architectures of BiOBr as a visible light-driven photocatalyst, Chem. Mater. 20 (2008) 2937–2941.
[23] J. Wang, Y. Yu, L. Zhang, Highly efficient photocatalytic removal of sodium pentachlorophenate with Bi_3O_4Br under visible light, App. Catal. B: Environ. 136–137 (2013) 112–121.
[24] S. Gazi, R. Ananthakrishnan, N.D.P. Singh, Photodegradation of organic dyes in the presence of [Fe(III)-salen]Cl complex and H_2O_2 under visible light irradiation, J. Hazard. Mater. 183 (2010) 894–901.
[25] R. Ananthakrishnan, S. Gazi, $[Ru(bpy)_3]^{2+}$ aided photocatalytic synthesis of 2-arylpyridines via Hantzsch reaction under visible irradiation and oxygen atmosphere, Catal. Sci. Technol. 2 (2012) 1463–1471.
[26] S. Gazi, R. Ananthakrishnan, Bromodimethylsulfonium bromide as a potential candidate for photocatalytic selective oxidation of benzylic alcohols using oxygen and visible light, RSC Adv. 2 (2012) 7781–7787.
[27] W.D. Wang, F.Q. Huang, X.P. Lin, *x*BiOI-(1-*x*)BiOCl as efficient visible-light-driven photocatalysts, Scr. Mater. 56 (2007) 669–672.
[28] C. Nasr, K. Vinodgopal, L. Fisher, S. Hotchandani, A.K. Chattopadhyay, P.V. Kamat, Environmental photochemistry on semiconductor surfaces. visible light induced degradation of a textile diazo dye, naphthol blue black, on TiO_2 nanoparticles, J. Phys. Chem. 100 (1996) 8436–8442.
[29] X.P. Lin, T. Huang, F.Q. Huang, W.D. Wang, J.L. Shi, Photocatalytic activity of a Bi-based oxychloride Bi_3O_4Cl, J. Phys. Chem. B 110 (2006) 24629–24634.
[30] K. Ishibashi, A. Fujishima, T. Watanabe, K. Hashimoto, Detection of active oxidative species in TiO_2 photocatalysis using the fluorescence technique, Electrochem. Commun. 2 (2000) 207–210.
[31] Z. Jia, F. Wang, F. Xin, B. Zhang, Simple solvothermal routes to synthesize 3D $BiOBr_xI_{1-x}$ microspheres and their visible-light-induced photocatalytic properties, Ind. Eng. Chem. Res. 50 (2011) 6688–6694.
[32] S.T. Huang, Y.R. Jiang, S.Y. Chou, Y.M. Dai, C.C. Chen, Synthesis, characterization, photocatalytic activity of visible-light-responsive photocatalysts BiO_xCl_y/BiO_mBr_n by controlled hydrothermal method, J. Mol. Catal. A: Chem. 391 (2014) 105–120.
[33] N.M. Dimitrijevic, B.K. Vijayan, O.G. Poluektov, T. Rajh, K.A. Gray, H. He, P. Zapol, Role of water and carbonates in photocatalytic transformation of CO_2 to CH_4 on titania, J. Am. Chem. Soc. 133 (2011) 3964–3971.
[34] L. Chen, S.F. Yin, S.L. Luo, R. Huang, Q. Zhang, T. Hong, P.C.T. Au, $Bi_2O_2CO_3$/BiOI photocatalysts with heterojunctions highly efficient for visible light treatment of dye-containing wastewater, Ind. Eng. Chem. Res. 51 (2012) 6760–6768.
[35] X. Xiao, R. Hao, M. Liang, X. Zuo, J. Nan, L. Li, W. Zhang, One-pot solvothermal synthesis of three-dimensional (3D) BiOI/BiOCl composites with enhanced visible-light photocatalytic activities for the degradation of bisphenol-A, J. Hazard. Mater. 233–234 (2012) 122–130.
[36] S. Shenawi-Khalil, V. Uvarov, S. Fronton, I. Popov, Y. Sasson, A novel class of heterojunction photocatalysts with highly enhanced visible light photocatalytic performances: yBiO(Cl_xBr_{1-x})-(1-y) bismuth oxide hydrate, Appl. Catal. B: Environ. 117–118 (2012) 148–155.
[37] S. Shenawi-Khalil, V. Uvarov, S. Fronton, I. Popov, Y. Sasson, A novel heterojunction BiOBr/bismuth oxyhydrate photocatalyst with highly enhanced visible light photocatalytic properties, J. Phys. Chem. C 116 (2012) 11004–11012.
[38] H. Fu, C. Pan, W. Yao, Y. Zhu, Visible-light-induced degradation of rhodamine B by nanosized Bi_2WO_6, J. Phys. Chem. B 109 (2005) 22432–22439.
[39] S. Kim, W. Choi, Kinetics and mechanisms of photocatalytic degradation of $(CH_3)_nNH_{4-n}^+$ ($0 \le n \le 4$) in TiO_2 suspension: the role of OH radicals, Environ. Sci. Technol. 36 (2002) 2019–2025.
[40] X. Zhu, J. Zhang, F. Chen, Study on visible light photocatalytic activity and mechanism of spherical $Bi_{12}TiO_{20}$ nanoparticles prepared by low-powder hydrothermal methods, Appl. Catal. B: Environ. 102 (2011) 316–322.
[41] K. Yu, S. Yang, C. Liu, H. Chen, H. Li, C. Sun, S.A. Boyd, Degradation of organic dyes via bismuth silver oxide initiated direct oxidation coupled with sodium bismuthate based visible light photocatalysis, Environ. Sci. Technol. 46 (2012) 7318–7326.
[42] F.D. Mai, C.S. Liu, J.L. Chen, C.C. Chen, Photodegradation of methyl green using visible irradiation in ZnO suspensions. Determination of the reaction pathway and identification of intermediates by a high-performance liquid chromatography-photodiode array-electrospray ionization-mass spectrometry method, J. Chromatogr. A. 1189 (2008) 355–365.
[43] M.C. Yin, Z.S. Li, J.H. Kou, Z.G. Zou, Mechanism investigation of visible light-induced degradation in a heterogeneous TiO_2/eosin Y/rhodamine B system, Environ. Sci. Technol. 43 (2009) 8361–8366.
[44] L.S. Zhang, K.H. Wong, H.Y. Yip, C. Hu, J.C. Yu, C.Y. Chan, P.K. Wong, Effective photocatalytic disinfection of *E. coli* K-12 using AgBr–Ag–Bi_2WO_6 nanojunction system irradiated by visible light: the role of diffusing hydroxyl radicals, Environ. Sci. Technol. 44 (2010) 1392–1398.
[45] S.G. Meng, D.Z. Li, M. Sun, W.J. Li, J.X. Wang, J. Chen, X.Z. Fu, G.C. Xiao, Sonochemical synthesis, characterization and photocatalytic properties of a novel cube-shaped $CaSn(OH)_6$, Catal. Commun. 12 (2011) 972–975.
[46] G. Li, K.H. Wong, X. Zhang, C. Hu, J.C. Yu, R.C.Y. Chan, P.K. Wong, Degradation of acid orange 7 using magnetic AgBr under visible light: the roles of oxidizing species, Chemosphere 76 (2009) 1185–1191.
[47] H.J. Fan, C.S. Lu, W.L.W. Lee, M.R. Chiou, C.C. Chen, Mechanistic pathways differences between P25-TiO_2 and Pt-TiO_2 mediated CV photodegradation, J. Hazard. Mater. 185 (2011) 227–235.
[48] Y. Li, H. Zhang, X. Hu, X. Zhao, M. Han, Efficient visible-light-induced photocatalytic activity of a 3D-ordered titania hybrid photocatalyst with a core/shell structure of dye-containing polymer/titania, J. Phys. Chem. C. 112 (2008) 14973–14979.
[49] X. Xiao, C. Xing, G. He, X. Zuo, J. Nan, L. Wang, Solvothermal synthesis of novel hierarchical $Bi_4O_5I_2$ nanoflakes with highly visible light photocatalytic performance for the degradation of 4-tert-butylphenol, Appl. Catal. B: Environ. 148–149 (2014) 154–163.